

1 **Geology and Geochemistry of Noachian Bedrock and**
2 **Alteration Events, Meridiani Planum, Mars:**
3 **MER Opportunity Observations**

4 David W. Mittlefehldt¹, Ralf Gellert², Scott vanBommel^{2,3}, Raymond E. Arvidson³, James W.
5 Ashley⁴, Benton C. Clark⁵, Larry S. Crumpler⁶, William H. Farrand⁵, Matthew P. Golombek⁴,
6 John A. Grant⁷, Richard V. Morris¹, Christian Schröder⁸

7 ¹Mail code XI3, Astromaterials Research Office, NASA/Johnson Space Center, Houston, Texas
8 77058, USA.

9 ²Department of Physics, University of Guelph, Guelph, ON N1G2W1, Canada.

10 ³Department of Earth and Planetary Sciences, Washington University in Saint Louis, Saint Louis,
11 Missouri 63130, USA.

12 ⁴Jet Propulsion Laboratory, California Institute of Technology, Pasadena, California 91109,
13 USA.

14 ⁵Space Science Institute, 4765 Walnut St., Suite B, Boulder, Colorado 80301, USA.

15 ⁶New Mexico Museum of Natural History and Science, 1801 Mountain Rd NW, Albuquerque,
16 New Mexico 87104, USA.

17 ⁷Smithsonian Institution, NASM CEPS, 6th at Independence Ave. SW, Washington, DC 20560,
18 USA.

19 ⁸Biological and Environmental Sciences, University of Stirling, Stirling FK9 4LA, Scotland, UK.
20

21 **Abstract** We have used Mars Exploration Rover Opportunity data to investigate the origin and
22 alteration of lithic types along the western rim of Noachian-aged Endeavour crater on Meridiani
23 Planum. Two geologic units are identified along the rim. The Shoemaker formation consists of
24 two types of polymict impact breccia: clast-rich with coarser clasts in upper units; clast-poor
25 with smaller clasts in lower units. Comparison with observations at terrestrial craters show that
26 the lower units represent more distal ejecta from one or more earlier impacts, and the upper units
27 are ejecta from Endeavour crater. Both are mixtures of target rocks of basaltic composition.
28 Subtle compositional differences are caused by differences in post-impact alteration along the
29 crater rim. The lower Shoemaker units and the Matijevic formation represent pre-Endeavour
30 geology, which we equate with the regionally mapped Noachian subdued cratered unit. An
31 alteration style unique to these rocks is formation of Si- and Al-rich vein-like structures
32 crosscutting outcrops, and formation of smectite. Post-Endeavour alteration is dominated by
33 sulfate formation. Rim-crossing fracture zones include regions of alteration that produced Mg-
34 sulfates as a dominant phase, plausibly closely associated in time with the Endeavour impact.
35 Calcium-sulfate vein formation occurred over an extended time period, including pre-Endeavour
36 impact and after the Endeavour rim had been substantially degraded, likely after deposition of
37 the Burns formation that surrounds and embays the rim. Differences in Mg, Ca and Cl
38 concentrations on rock surfaces and interiors indicate mobilization of salts by transient water that
39 has occurred recently and may be ongoing.

40 **Plain Language Summary** Data returned by the Mars Exploration Rover Opportunity was used
41 to investigate rock origins along the western rim of Endeavour crater on Meridiani Planum,
42 Mars. The Shoemaker formation consists of impact-formed breccia of two types: coarser-grained
43 upper subunits and finer-grained lower subunits. The lower units represent ejecta from one or
44 more older, more distant craters, while the upper units are ejecta from Endeavour crater. Subtle
45 compositional differences are caused by differences in post-impact alteration along the crater
46 rim. The lower Shoemaker units represent part of the pre-Endeavour geology. An alteration style
47 unique to the pre-Endeavour rocks is formation of Si- and Al-rich structures crosscutting
48 bedrock. Post-Endeavour alteration is dominated by sulfate formation. Fracture zones in the rim
49 include regions of alteration that produced Mg-sulfates as a dominant phase, plausibly closely
50 associated in time with the Endeavour impact. Calcium-sulfate vein formation occurred over an
51 extended time period, some before the Endeavour impact and some much later, likely after
52 deposition of the sulfate-rich sandstones of Meridiani Planum. Differences in composition of
53 rock surfaces and interiors indicate that mobilization of salts by transient water has occurred
54 recently and may be ongoing on Mars.

55 **Keywords:** Mars geology; Mars geochemistry; Noachian crust; Endeavour crater; Mars
56 Exploration Rover mission

57

58 **1. Introduction**

59 Mars Exploration Rover (MER) Opportunity explored the geology of Meridiani Planum
60 within Arabia Terra for 5111 Sols (Mars days), from the date of landing on 25 January 2004
61 through the loss of signal on 19 June 2018, which was caused by a global dust storm that choked
62 off her solar energy supply. Through Sol 2680, corresponding to the first seven and a half Earth
63 years of the mission, Opportunity traversed the hematite plains making observations of sulfate-
64 rich sedimentary rocks and associated hematite-concretion surface-lag (Arvidson et al., 2011;
65 Squyres et al., 2006a). These constitute the upper layers of the Late Noachian/Early Hesperian
66 Meridiani upper etched unit and the Early Hesperian hematite unit (Hynek & Di Achille, 2017).

67 Opportunity began exploring the northwestern rim of Endeavour crater on Sol 2681 (09
68 Aug. 2011). Endeavour crater is a 22 km diameter complex impact structure (Fig. 1a) formed in
69 Noachian aged materials that predate the embaying sulfate-rich sedimentary rocks (Arvidson et
70 al., 2014; Hynek et al., 2002). The Endeavour crater rim was chosen as a target because the rocks
71 record an ancient epoch in martian history, and because phyllosilicate minerals were identified
72 on portions of the rim from orbit (Wray et al., 2009). The latter demonstrate that a period of
73 aqueous alteration is recorded in the rocks. Exploration of Endeavour crater rim directly
74 addressed one of the main goals of the MER mission: to explore regions and associated rocks
75 and soils where water might have been present and to make assessments regarding past
76 habitability (Squyres et al., 2003).

77 Post-impact erosion has degraded the Endeavour crater rim into a series of rim segments
78 (Grant et al., 2016; Hughes et al., 2019). The first rim segment explored by Opportunity was the
79 ~700 m long Cape York that rises ~10 m above the surrounding plains (Fig. 1b) (Grant et al.,
80 2016). Near-infrared spectra from the Compact Reconnaissance Imaging Spectrometer for Mars
81 (CRISM) instrument indicated the presence of phyllosilicates in this region (Wray et al., 2009).
82 Investigations with the rover science payload revealed that the orbitally resolved phyllosilicates
83 correspond to ferric smectite occurring roughly midway down the inboard (southeastern) side of
84 Cape York (Fig. 1b; online supplement Fig. L01) (Arvidson et al., 2014). At that location, the
85 thin, fine-grained clastic Matijevic formation is exposed. It was identified as being part of the
86 pre-Endeavour basement and the host of the ferric smectite (Arvidson et al., 2014; Crumpler et
87 al., 2015). Shoemaker Ridge forms the topographic expression of Cape York and is composed of
88 Noachian polymict impact breccias formed by the Endeavour impact; these constitute the
89 Shoemaker formation (Crumpler et al., 2015; Squyres et al., 2012). The Grasberg formation, a
90 thin, very-fine-grained airfall unit that drapes the lower, eroded pediment surfaces of Endeavour
91 rim segments, also occurs on Cape York (Crumpler et al., 2015; Grant et al., 2016).

92 Cape Tribulation is a major rim segment south of Cape York (Fig. 1c). This segment also
93 presented evidence for the localized presence of phyllosilicates, particularly in the region of a
94 large, rim-transecting valley named Marathon Valley (Fig. 1d; online supplement Fig. L04) (Fox
95 et al., 2016; Wray et al., 2009). Exploration of Cape Tribulation began at its northern tip and
96 continued to Perseverance Valley, which cuts the rim between the southern terminus of Cape
97 Tribulation and the next rim segment, Cape Byron (Fig. 1e; online supplement Fig. L09). For

most of the traverse, Opportunity explored rocks on the outboard (western) side of Cape Tribulation, but major science campaigns were done in Marathon and Perseverance Valleys. Both valleys cut the rim and expose bedrock of the lower stratigraphic section. The focus of the discussion takes over from where Mittlefehldt et al. (2018a) left off. This includes data for all rock targets analyzed from Sol 3935 (17 Feb. 2015) through the last contact science measurements on Sol 5105 (03 June 2018). We also discuss the erratic block Marquette Island which was discovered on the hematite plains on Sol 2055 (04 Nov. 2009). This block is interpreted to be an ejecta block of the Noachian crust that predates sedimentary rocks of the hematite plains (Arvidson et al., 2011). Soil analyses are not discussed in detail but are utilized to help interpret relationships among rock compositions.

The instruments of the Athena payload (Squyres et al., 2003) that were used to investigate the geology and geochemistry of the region include: the Alpha Particle X-ray Spectrometer (APXS; Rieder et al., 2003), the Microscopic Imager (MI; Herkenhoff et al., 2003), the Panoramic Camera (Pancam; Bell et al., 2003) and the Rock Abrasion Tool (RAT; Gorevan et al., 2003). These were supported by imaging from the engineering cameras – Navigation Cameras (Navcam) and front and rear Hazard Avoidance Cameras (Hazcam) (Maki et al., 2003). The MIMOS II Mössbauer Spectrometer (Klingelhöfer et al., 2003) was still operational during observations on Marquette Island; we include data from it in that discussion.

The major focus of this paper is on the compositional information returned by the APXS and its use in defining alteration processes. These data are put into geological context using information derived from orbital and *in-situ* mapping. Pancam and Navcam images are used to interpret outcrop textures and structures, and Pancam spectra are used to help constrain mineralogy. The micro-textures of the rocks are interpreted from MI images. The Mars observations are compared to rocks from terrestrial craters and tied to information derived from cratering mechanics studies. The observations discussed here are developed into a geological and alteration history for the region around Endeavour crater.

2. The APXS Dataset

The APXS determines chemical compositions of rocks and soils using X-ray spectroscopy after irradiation with energetic alpha particles and X-rays. It resembles a combination of the laboratory methods of X-ray fluorescence spectrometry (XRF) and particle induced X-ray emission spectrometry (Rieder et al., 2003). The analysis field of view has a diameter of 38 millimeters, but the instrument response is strongest in the central region. Concentrations are extracted from the X-ray spectra using the empirical method described in Gellert et al. (2006). Complete results for 287 analyses of rocks and soils from the Endeavour crater rim and 2σ precision errors of the peak areas are reported in Table 1. Of these, 141 analyses were previously unpublished. Locations for all analyses presented in Table 1 except for Marquette Island and soils far from Endeavour rim are shown in the online supplement. [Note to reviewers: All data tables will be hosted in an online data repository. An Excel file with these tables was uploaded for review purposes.] The table also includes the typical relative accuracy of the method, which is taken from Table 1 of Gellert et al. (2006), and the typical relative precision of the measurements based on a representative Shoemaker formation rock analysis, taken from

139 Table S1 of Mittlefehldt et al. (2018a). A detailed discussion of the methodology used here is
140 presented in Mittlefehldt et al. (2018a).

141 **3. Geological Context**

142 The basement in the region explored by Opportunity consists of the Early to Middle
143 Noachian subdued cratered unit (Hynek & Di Achille, 2017). This unit is interpreted to be
144 composed of primary (volcanic, pyroclastic) and secondary (impact breccia, fluvial and aeolian
145 sedimentary) lithic types (Hynek & Di Achille, 2017). This highlands unit is overlain by three
146 Meridiani etched plains units; the lower two are Middle to Late Noachian in age; the topmost
147 unit is Late Noachian/Early Hesperian in age (Fig. 2). These units are interpreted to be aeolian
148 and/or volcanic deposits (Hynek & Di Achille, 2017; Hynek & Phillips, 2008). The Burns
149 formation is the uppermost lithified section of the etched unit stratigraphy, and is sulfate-rich
150 aeolian sandstone (e.g., Grotzinger et al., 2005; Squyres and Knoll, 2005; Squyres et al., 2006a).

151 Endeavour crater is northeast of the ~160 km-diameter Miyamoto crater (Grant et al.,
152 2016; Newsom et al., 2003) which is in the subdued cratered unit (Fig. 2a). Miyamoto crater is
153 an ancient, degraded crater partially filled by Meridiani etched plains units on the north-northeast
154 side. Morphologic evidence points to fluvial erosion having impacted the landscape outside and
155 inside the crater (Newsom et al., 2003, 2010). Iron-Mg-rich smectite phases are located on the
156 western floor of Miyamoto crater (Wiseman et al., 2008). Bopolu crater, 19 km in diameter,
157 impacted on the Meridiani etched plains units that partially fill Miyamoto crater. This is a fairly
158 pristine crater that exposes altered Noachian basement in its walls (Grant et al., 2016), further
159 testifying to ancient alteration of the Miyamoto crater floor rocks. Alteration in this region is
160 thought to have been a response to the hydrological environment of western Arabia Terra in
161 which groundwaters from the highlands to the south emerged in local topographic lows and
162 caused alteration of the bedrock (Andrews-Hanna & Lewis, 2011; Andrews-Hanna et al., 2007).
163 The Endeavour impact occurred ~20 km outside the rim of Miyamoto crater within the region of
164 its continuous ejecta deposit. The pre-impact terrain would have included polymict breccias from
165 that earlier impact and these could have been altered as observed for floor rocks in Miyamoto
166 crater (Wiseman et al., 2008). Iazu crater is a 6.8 km-diameter structure ~25 km south of
167 Endeavour crater (Fig. 2b). It is a relatively pristine, simple bowl-shaped crater surrounded by a
168 pedestal of ejecta. That latter is thought to be the result of wind erosion preferentially removing
169 the less resistant Burns formation rocks (Powell et al., 2017). Iazu crater exposes Noachian-aged,
170 ferric-smectite-bearing altered basaltic-composition basement below Burns formation in its
171 crater walls (Powell et al., 2017), further establishing that the pre-impact terrain for Endeavour
172 crater consisted of ancient, altered rocks.

173 The stratigraphy in the region of Endeavour crater rim is divided into four formations
174 which are, oldest to youngest; the Matijevic, Shoemaker, Grasberg and Burns formations
175 (Crumpler et al., 2015). The Matijevic formation is part of the pre-Endeavour terrain exposed at
176 the inboard side of Cape York (online supplement Fig. L01), and is a fine-grained clastic rock
177 (Arvidson et al., 2014). The limited exposures prohibit firm conclusions regarding its origin, but
178 its morphology and texture are consistent with formation as volcanic ash or distal impact ejecta
179 (Crumpler et al., 2015). Polymict impact breccias of the Shoemaker formation comprise the

180 major lithic type of the Endeavour crater rim on the segments explored by Opportunity and
181 underpin the topographic expressions of the rim segments (Crumpler et al., 2015; Squyres et al.,
182 2012). The Shoemaker formation, the major focus of this communiqué, is discussed in Section 4.
183 A continuous bench of bright rock encircles Cape York (online supplement Fig. L01), partially
184 surrounds the margin of Cape Tribulation and is discernable in High Resolution Imaging Science
185 Experiment (HiRISE) images of other rim segments of Endeavour crater (e.g., Grant et al.,
186 2016). This bench is part of the Grasberg formation, a very-fine-grained clastic deposit that
187 drapes the eroded lower slopes of rim segments (Crumpler et al., 2015). The Grasberg formation
188 is a thin, altered airfall deposit with possibly a weathering cap that is of volcanic or impact origin
189 and might be regional in extent (Crumpler et al., 2015). New analyses of two Grasberg formation
190 rocks are included in Table 1, but we do not discuss them; the composition of this formation is
191 discussed in Mittlefehldt et al. (2018a). Finally, the Burns formation is dominated by sulfate-rich
192 sandstones with a minor component of mudstone (e.g., Edgar et al., 2012; Grotzinger et al.,
193 2005). Most of the sandstones are aeolian in origin, but there are some aqueous facies that
194 bespeak local fluvial reworking and rare mudstones indicate localized deposition in quiet water,
195 possibly a lacustrine setting (Edgar et al., 2012, 2014; Grotzinger et al., 2005, 2006; Hayes et al.,
196 2011). Unconformities separate all formations.

197 There are several lithic types in the region that do not occur as mappable formations that
198 are covered here under the rubric “dark rocks.” These include dark-rock boulder-float similar to
199 those discussed previously (Mittlefehldt et al., 2018a), two types of scattered, more massive,
200 fine-grained rock that we refer to as blue- and purple-rock erratics based on their appearance in
201 Pancam false color images, and three types of dark rock from Perseverance Valley. Finally, we
202 encountered a dark-rock block – Marquette Island – on the hematite plains roughly 11,800
203 meters from the Endeavour rim. Marquette Island is interpreted to be an ejecta fragment from the
204 Noachian crust (Arvidson et al., 2011), and has a general compositional similarity to
205 Adirondack-class basalts from Gusev crater but likely contains a higher fraction of light elements
206 (H, C, O) than found for other rocks (Mittlefehldt et al., 2010). Because this might indicate
207 unusual alteration, we discuss it here.

208 4. Shoemaker Formation

209 Shoemaker formation rocks are polymict impact breccias which we interpreted as being
210 ejecta from Endeavour crater (Arvidson et al., 2014; Crumpler et al., 2015; Mittlefehldt et al.,
211 2018a; Squyres et al., 2012). However, our later investigations in Marathon and Perseverance
212 Valleys presented geological evidence that some subunits of the Shoemaker formation pre-date
213 the Endeavour impact (Mittlefehldt et al., 2018b, 2019a). We present that evidence in this section
214 and refine our interpretation of the Shoemaker formation. We present our compositional
215 information on Shoemaker formation rock targets and discuss them in relation to our
216 interpretation of subunit origins. Further, we discuss alteration features in the Shoemaker
217 formation from Marathon and Perseverance Valleys, and compositional differences between
218 surfaces and interiors of several rocks. The online supplement contains locator images for all
219 Pancam images shown and rock targets called-out.

220 **4.1 Stratigraphy, Texture, Morphology and Origin of Subunits**

221 The Shoemaker formation is the major rock unit of the rim. It originally formed the
222 continuous ejecta deposit surrounding Endeavour crater, but subsequent degradation has reduced
223 its areal coverage (Grant et al., 2015). It is divided into three members on Cape York (Figs. 15,
224 17 of Crumpler et al., 2015). The Greeley Haven member is the thickest and uppermost subunit
225 of the Shoemaker formation, and is a coarse, clast-rich polymict breccia with multi-cm-sized
226 dark clasts in a brighter, fine-grained matrix (Fig. 3a) (Arvidson et al., 2014; Crumpler et al.,
227 2015; Mittlefehldt et al., 2018a; Squyres et al., 2012). The Chester Lake member was
228 encountered on the southern tip of Cape York when we began exploring the rim (online
229 supplement Fig. L01) (Crumpler et al., 2015). Copper Cliff is the lowermost member and
230 unconformably overlies the pre-impact Matijevic formation (online supplement Fig. L01)
231 (Crumpler et al., 2015). It is a transitional breccia that shows some textural and compositional
232 characteristics of the underlying Matijevic formation (Arvidson et al., 2014; Crumpler et al.,
233 2015; Mittlefehldt et al., 2018a). Mittlefehldt et al. (2018a) concluded that the Copper Cliff
234 member was formed by mixing Endeavour ejecta with material eroded from the pre-impact
235 paleosurface via a ballistic erosion-sedimentation process (e.g., Hörz et al., 1983; Oberbeck,
236 1975).

237 The Shoemaker formation is subdivided into upper and lower subunits on Cape
238 Tribulation, but no attempt was made to correlate them with the three members defined on Cape
239 York. However, most of the breccias on Cape Tribulation discussed in Mittlefehldt et al. (2018a)
240 are morphologically and texturally like the Greeley Haven member on Cape York (e.g., Fig. 3b).
241 These are assigned to the upper Shoemaker subunit on Cape Tribulation (Crumpler et al., 2019,
242 2020). The area around the Spirit of Saint Louis feature and the floor of Marathon Valley contain
243 breccias that have lower abundances of clasts and typically smaller clasts (Figs. 3d, e), which are
244 mapped as two subunits (lower-1 and lower-2) of the Shoemaker formation (Crumpler et al.,
245 2019; 2020). Previously, we did not recognize subunits of the Shoemaker formation on Cape
246 Tribulation, although we noted that breccias at Cook Haven and at the Hueytown fracture zone
247 showed some similarity to breccias now mapped as lower Shoemaker in Marathon Valley (Fig.
248 3c) (Mittlefehldt et al., 2018a). A single lower subunit of the Shoemaker formation is also
249 recognized in the lower elevation of Perseverance Valley (Fig. 3f) (Crumpler et al., 2019; 2020).

250 We now identify the lower Shoemaker formation subunits as distal impact ejecta from
251 one or more pre-Endeavour craters, and thus they are not correlative with the Shoemaker
252 formation on Cape York. The arguments supporting this are based on comparing upper and
253 lower Shoemaker rocks with an analysis of experimental and observational work on impact
254 processes (Oberbeck, 1975) plus studies of terrestrial caters (e.g., Hörz et al., 1983; Mader &
255 Osinski, 2018; Shoemaker, 1963).

256 As summarized by Oberbeck (1975), ejecta fragments from a crater are launched at
257 differing angles and velocities, but all follow ballistic trajectories. The earliest ejecta fragments
258 are derived from closer to the pre-impact surface, nearer the impact point, and are launched at the
259 highest angles and velocities (Fig. 4). Conversely later ejecta fragments are generally derived
260 from deeper in the target zone, further from the impact point, and are launched at lower angles

and velocities. This results in a conical ejecta curtain that sweeps outward, first along with the transient crater margin as the crater grows and then over the pre-impact surface once the final transient crater size is reached. As the ejecta curtain moves outward the largest and slowest fragments are at its base; the fastest and smallest ones at its top. Close to the transient crater rim, fragments impact the surface at shallower angles, lower velocities and fragment sizes are larger on average than is the case for the distal edge of the ejecta deposit (solid arrow – schematic ejecta fragment velocity vectors; Fig. 4 insets). Furthermore, the impacting ejecta fragments cause ballistic erosion and sedimentation on the pre-impact surface that result in mixing pre-impact rock with ejected clasts. This process is more effective at greater distances because of the combined steeper impact angles and higher velocities of the ejecta fragments. The final dregs of energy are dissipated through outward, ground-hugging flow of the mixture of ejecta fragments and eroded bedrock/soil (open arrow – schematic ejecta deposit velocity vectors; Fig. 4 insets). The results are polymict breccias that have larger average clast sizes and lower matrix contents close to the tectonic rim of a large crater than at the distal edge of the ejecta deposit.

Detailed geological work on terrestrial craters, especially the extensive studies of the Bunte Breccia of the Ries Crater, offer specific examples of ejecta deposits that match the synopsis presented by Oberbeck (1975). The Ries Crater is of similar size to Endeavour crater, ~26 km diameter vs. ~22 km, is well-preserved and thus is an excellent terrestrial analog. Hörz et al. (1983) summarized petrologic work done on cores taken at numerous locations at different radial ranges through the Bunte Breccia and noted that there is no systematic vertical trend in the grain sizes of matrix components, nor is there a systematic vertical trend in clast size. The cores are chaotic mixtures of clasts and matrix throughout their length at any given location. Mader & Osinski (2018) similarly noted that the polymict breccias of the ~28 km diameter Mistastin Lake impact structure are poorly sorted, and Shoemaker (1963) described the ejecta surrounding the simple, bowl-shaped, 1.2 km diameter Meteor Crater as consisting of unsorted debris from <1 μm to >30 m in size. Hörz et al. (1983) identified a systematic trend of decreasing average clast size with radial distance from the Ries Crater rim, and Shoemaker (1963) reported decreasing block size and frequency with increasing radial range from Meteor Crater. Hörz et al. (1983) do not specifically state that the clast/matrix ratio decreases with radial range, but this can be inferred from the observations that: (i) the amount of primary crater material in the ejecta decreases with radial range; and (ii) the matrix is >95% derived from ballistic erosion of the local surface. Thus, the geological evidence demonstrates that ejecta deposits are unsorted, chaotic breccias at individual locations that show systematic variations with radial range.

The textures of the upper and lower Shoemaker formation do not match those expected of ejecta from a single impact. We have the best stratigraphic control on Cape Tribulation in the region of Marathon Valley where the two lower subunits occur as the valley floor and around the Spirit of Saint Louis feature, while upper Shoemaker rocks form the bounding ridges (Fig. 5) (Crumpler et al. 2020). In Perseverance Valley the upper Shoemaker similarly overlies the lower Shoemaker (Crumpler et al., 2020). A systematically finer-grained and clast-poor breccia at the base of a coarser-grained, clast-rich breccia is inconsistent with formation as an ejecta deposit from a single impact event. Rather, the textures of the lower Shoemaker subunits are consistent

302 with formation from impacts that were more distant than that which produced the upper
303 Shoemaker.

304 Hence, the geologic evidence supports an origin of the lower Shoemaker subunits on
305 Cape Tribulation as distal ejecta from one or more impacts that predate Endeavour crater
306 formation. The ridge-forming upper Shoemaker is an ejecta deposit from the Endeavour impact.

307 On Cape York, the Copper Cliff member of the Shoemaker formation overlies the pre-
308 impact Matijevic formation and was mapped as a transitional breccia (Crumpler et al., 2015).
309 The Copper Cliff member shows some textural and compositional similarities to the Matijevic
310 formation (Crumpler et al., 2015; Mittlefehldt et al., 2018a), which we attributed to ballistic
311 erosion and sedimentation processes as the Endeavour ejecta impacted the pre-impact surface
312 (Mittlefehldt et al., 2018a). Although mapped as a transitional breccia, the Copper Cliff member
313 is nevertheless a coarse breccia, the transitional character being imparted by inclusion of 1-2 mm
314 spherules like those that are present in the Matijevic formation (Arvidson et al., 2014; Crumpler
315 et al., 2015). Thus, the geological evidence does not support a pre-Endeavour origin for the
316 Copper Cliff member, and all Shoemaker formation breccias on Cape York are Endeavour
317 deposits.

318 **4.2 Composition**

319 We have done 138 analyses of Shoemaker formation rocks, including those discussed in
320 Mittlefehldt et al. (2018a). Of these, 29 analyses were done on brushed targets, while 18 were on
321 abraded targets. Some of the latter were cases where the abrasion was of low quality either
322 because the activity faulted-out before completion, or topography of the surface was too great to
323 result in a good abrasion circle at the planned depth. We consider that 13 analyses were on well-
324 abraded targets. The 138 analyses represent 68 different rocks.

325 We have grouped the Shoemaker formation APXS targets according to geologic map
326 units (Table 1) (Crumpler et al., 2015; 2020). The upper Shoemaker is undivided on Cape
327 Tribulation; their geographic locations are noted on Table 1. A region mapped as Shoemaker
328 lower-1 in Marathon Valley presented spectral evidence for the presence of Fe-Mg smectite in
329 CRISM data (Fox et al., 2016), and four analyses from the region showing the strongest smectite
330 signal are grouped separately. The Parral target is an ~5 cm rock fragment in a region of bedrock
331 fragments on a dark sand substrate. The Zacatecas target from this region consists of mixed small
332 bedrock fragments and dark sand. Both are listed with the upper Shoemaker rocks, but the latter
333 might better be considered a composite soil (see Cabrol et al., 2014), and as discussed below,
334 Parral is plausibly a cobble of lower Shoemaker.

335 Shoemaker formation rocks are essentially basaltic in composition and are like an
336 estimated mean martian crust composition (Taylor & McLennan, 2009) (Fig. 6). Compositional
337 variations within the suite generally are minor. Although compositions of the breccias from
338 different locations and/or subunits substantially overlap for many elements, there are
339 nevertheless systematic differences for some elements. Thus, on Cape York the average FeO
340 content increases in the sequence Copper Cliff, Greeley Haven, Chester Lake members, and
341 Shoemaker formation rocks have systematically higher Fe/Mn on Cape Tribulation than on Cape

342 York (Mittlefehldt et al., 2018a). Most of the compositional differences observed among
343 subunits of the Shoemaker formation are in the volatile elements (S, Cl, Br; Fig. 7) that have
344 been labile in the recent Martian environment (see Mittlefehldt et al., 2019b, and references
345 therein), and in the mobile elements (P, Mn, Ni, Zn) that were mobilized by localized alteration
346 events (Arvidson et al., 2016; Jolliff et al., 2019; Mittlefehldt et al., 2018a, 2019b). Table 2 gives
347 the mean compositions plus uncertainties for subunits of the Shoemaker formation. For the three
348 volatile elements the compositional data are averaged. For all other elements, the analyses are
349 normalized to a SO₃-, Cl- and Br-free basis, and the normalized data are averaged. Excluding the
350 volatile elements, the averages of different subunits for most of the elements overlap within
351 uncertainty.

352 Because variations in composition within the Shoemaker formation are subtle,
353 multivariate statistical techniques offer the best method for revealing compositional associations.
354 We used Agglomerative Hierarchical Cluster Analysis (AHCA) to group observations (APXS
355 targets) by similarities in variables (elements). We used Ward's minimum variance method for
356 defining cluster linkages as it results in little within-cluster distance (synonymous with little
357 internal dissimilarity). We used the Euclidean distance metric, and centroids were determined
358 using the sum of distances. Element/Si mole ratios were used as variables to minimize problems
359 associated with the closure restraint caused by forcing the APXS data to equal 100% (Chayes,
360 1971), and following Aitchison (1994), we modeled log(element/Si) rather than simple mole
361 ratios. We included most of the rock types formed during or before the Endeavour impact: (i)
362 Shoemaker formation targets; (ii) Matijevic formation matrix, spherule-rich and veneer targets;
363 (iii) dark-rock boulder-float; (iv) blue-rock erratics; (v) basaltic outcrops from Perseverance
364 Valley; (vi) basaltic rocks from the central fracture zone in Perseverance Valley; (vii) dark rocks
365 from Wdowiak Ridge; (viii) boxwork vein targets from the Matijevic fm.; (ix) red-zone rocks
366 from the Marathon Valley region; (x) pitted rocks from Perseverance Valley; and (xi) purple-
367 rock erratics. The latter four groups are generally silica-rich and compositionally distinct from all
368 other rocks along the rim (Fig. 6). We have excluded Matijevic formation, Shoemaker formation
369 and red-zone targets that contained CaSO₄ veins from the modeling.

370 We included soil samples in our AHCA modeling to help evaluate the effects partial soil
371 cover might have on the compositions of untreated surfaces. The types of soils modeled are: (i)
372 dark sand composed of the fine-sand-sized particles that actively saltate in the current
373 environment; (ii) bright soils composed of deposits of airfall dust; and (iii) composite soils
374 composed of mixtures of fine to coarse materials (Cabrol et al., 2014). For the composite soils,
375 we included only those lying on Shoemaker formation substrate as judged by geological maps.
376 For dark-sand and bright-soil targets, we used those from the entire rover traverse. This resulted
377 in 237 analyses being modeled. Table 3 gives the element/Si mole ratios for analyses used in the
378 AHCA modeling.

379 We excluded the volatile elements S, Cl, and Br from the analyses because, to the extent
380 possible, we wish to focus on the silicate compositions of the rocks. Sulfur and Cl are variable
381 within the suite and are at wt% concentration levels (Table 1; Fig. 7). This can cause targets with
382 very similar silicate compositions to occupy dissimilar clusters if S/Si and Cl/Si are included in
383 the modeling. We included the mobile elements P, Mn, Ni and Zn in the first model run to help

384 evaluate which targets might contain subtle signatures of alteration processes and ran a second
385 model excluding these elements to evaluate the impact of alteration on the rocks.

386 We forced the calculation to return 20 clusters in order to obtain finer granularity on the
387 results, and merge clusters at higher levels by inspection of the dendrogram and cluster
388 memberships to yield geologically interpretable results. A cluster hierarchy matrix summarizing
389 the distributions of different rock types in the clusters for the first model run is given in Table 4a;
390 the dendrogram is given in Fig. 8. The cluster hierarchy matrix for the second model run is given
391 in Table 4b. The observations axis shows individual analyses and linkages between them
392 grouped in color-coded clusters. The inset shows an expanded view of 16-member cluster 1.
393 Individual observations are joined with other observations (or linked observations) at distances
394 (degrees of dissimilarity) indicated by the cross linkages. The labeled cluster members are the
395 two most similar members of this cluster (linked at the smallest distance). These are two analyses
396 of the abraded Azilda2 target in the Matijevic formation, one done before and one after the
397 abrasion hole was brushed to clear out debris. Cluster 1 is fully defined when all observations are
398 finally joined at the greatest distance (highest degree of dissimilarity) – the linkage at a distance
399 of ~1.11. This level of dissimilarity for cluster 1 was set by our arbitrary requirement that the
400 analysis return 20 clusters.

401 We discuss the AHCA models at the most dissimilar level and go deeper as needed. Four
402 major clusters are evident in Fig. 8: A, including clusters 1-7 (72 analyses); B, containing
403 clusters 8-11 (40 analyses); C, consisting of clusters 12-15 (91 analyses); and D, composed of
404 clusters 16-20 (34 analyses). Major cluster D links with ABC at a distance of 27.7, more than
405 twice the distance of the A-BC linkage (12.3). Major cluster D includes most analyses (63%) of
406 the four silica-rich lithic types shown in Fig. 6: silica-rich boxwork veins from the Matijevic
407 formation; the red-zone group; pitted rocks from Perseverance Valley; purple-rock erratics.
408 These will be discussed in section 4.3. All analyses of erratic rock Marquette Island are in cluster
409 15 of major cluster C; this rock is discussed in section 5. For the second AHCA model run, we
410 similarly group the 20 clusters into four major clusters and refer to them as I through IV (Table
411 4b) for clarity in the discussion. The distance of the last linkage separating major cluster IV from
412 the other is ~12.4, less than half the distance of the ABC-D linkage in the first model run (Fig.
413 8), which indicates that the mobile elements contribute importantly to the compositional
414 variability.

415 All soil targets in the first model occupy either cluster 6 or 14 (Table 4a) and most of the
416 soil targets in the second model run are in cluster 11 (Table 4b). All rock targets in these clusters
417 are untreated. Because of this, we consider their compositions to be possibly compromised and
418 they are discounted in the discussion that follows. Six untreated rocks are clustered with soils in
419 both model runs and are especially suspect.

420 For the first model run, analyses contained in major cluster A include 65% of the
421 Endeavour crater Shoemaker breccias, but none of the pre-Endeavour crater Shoemaker breccias.
422 It includes 57% of the Matijevic formation rocks (excluding the boxwork veins), 20% of the dark
423 basaltic rocks and 18% of the erratic rocks (Table 4a). Analyses contained in major cluster B
424 include 6% of the Endeavour crater Shoemaker formation breccias, 33% of the pre-Endeavour

425 Shoemaker breccias, the remainder of the Matijevic formation rocks, and none of the dark
426 basaltic or erratic rocks. Major cluster C includes 27% of the Endeavour crater Shoemaker
427 breccias, 64% of the pre-Endeavour Shoemaker breccias, none of the Matijevic formation
428 analyses, 13% of the dark basaltic rocks and 41% of the erratic rocks. Major cluster D includes
429 only 3% of the pre-Endeavour Shoemaker breccias, none of the Matijevic formation analyses,
430 67% of the dark basaltic rocks and 41% of the erratic rocks. The sole 2 Endeavour crater
431 Shoemaker breccia analysis in major cluster D is the anomalous target Sledge Island1.

432 There is a substantially different distribution of Endeavour and pre-Endeavour
433 Shoemaker formation breccias between the major clusters; most Endeavour Shoemaker breccias
434 are in major cluster A while most pre-Endeavour Shoemaker breccias are in major cluster C.
435 There is a geographic distinction for clustering amongst Endeavour crater Shoemaker breccias:
436 97% of those from Cape York are in major cluster A while 68% of those from Cape Tribulation
437 are in major cluster C. This latter fact suggests either that there was a different lithic mixture in
438 the ejecta deposited on Cape York than on Cape Tribulation or that alteration processes on the
439 two rim segments were different. The latter is supported by the second AHCA model run that
440 excluded the more mobile elements. In this model, Endeavour crater Shoemaker breccias from
441 Capes York and Tribulation are all dominantly (86-89%) in major cluster II (Table 4b). We
442 conclude that post-Endeavour alteration processes in the region of Cape York were different in
443 degree or style than those in the neighborhood of Cape Tribulation. We presaged this possibility
444 in Mittlefehldt et al. (2018a) where we noted that there was a systematic difference in Fe/Mn
445 ratios of Shoemaker formation breccias between those on Cape York and on Murray Ridge from
446 Cape Tribulation, and we noted that Mn was mobile during alteration.

447 When the mobile elements are excluded from the model, pre-Endeavour Shoemaker
448 breccias are mostly in major cluster II with the Endeavour crater Shoemaker breccias (Table 4b).
449 However, the pre-Endeavour Matijevic formation rocks are overwhelmingly in major cluster I.
450 Together, these results suggest that the Shoemaker breccias deposited by the Endeavour impact
451 are mostly composed of lithic materials like the lower Shoemaker, and rocks like the Matijevic
452 formation make up a minor proportion.

453 There are some textural similarities between the Copper Cliff member of the upper
454 Shoemaker and the Matijevic formation that are not observed for other members of the
455 Shoemaker formation on Cape York (Crumpler et al., 2015). The AHCA modeling we did
456 previously indicated a compositional connection between the Copper Cliff member and the
457 Matijevic formation that was not observed for other members of the Shoemaker formation
458 (Mittlefehldt et al., 2018a). We interpreted the compositional and textural evidence to establish
459 that the Copper Cliff member was formed by ballistic erosion and sedimentation processes
460 (Oberbeck, 1975) as Endeavour ejecta impacted and mixed with rocks on the pre-Endeavour
461 (locally Matijevic formation) surface (Mittlefehldt et al., 2018a). Here we reexamine the possible
462 connection between the Copper Cliff member and the Matijevic formation using our new AHCA
463 results on a larger data set. Our previous AHCA modeling using a different linkage method and
464 simple element/Si mole ratios, not log ratios. Use of the log ratios here will make the results
465 more robust against the closure problem (Aitchison, 1994).

466 The compositional connection between the Copper Cliff member and the Matijevic
467 formation is generally supported by our present modeling. In the first model which excludes the
468 volatile elements (S, Cl and Br), analyses of the Matijevic matrix (clastic rocks with few
469 spherules) and two analyses of veneer on the Matijevic surface are in cluster 1 as are 63% of the
470 Copper Cliff analyses (Table 4a). No other Shoemaker formation analyses are in cluster 1. The
471 remainder of the Copper Cliff analyses are in cluster 2, along with the other analyses of the
472 veneer. Two upper Shoemaker formation analyses are in cluster 2; anomalous rock Sledge
473 Island1 and Parral, which we argued above is plausibly lower Shoemaker. Analyses of the
474 spherule-rich targets in the Matijevic formation are in cluster 9, part of major cluster B, and thus
475 show no close compositional connection to the Copper Cliff member (or the other Matijevic
476 formation targets for that matter). When the mobile elements P, Mn, Ni and Zn are excluded
477 from the modeling, all matrix and spherule-rich Matijevic targets and three of five of the veneer
478 targets are in clusters 1 and 2, as are 63% of the Copper Cliff member analyses, but only two of
479 upper Shoemaker targets. The new AHCA modeling still indicates a compositional connection
480 between the Copper Cliff member and the underlying Matijevic formation and we conclude that
481 formation by ballistic erosion and sedimentation processes (Oberbeck, 1975) remains a good
482 model for understanding the Copper Cliff member.

483 We grouped four analyses of two targets (York and Jean Baptiste Deschamps) separately
484 for the purposes of AHCA modeling, and the results show that they are compositionally
485 distinctive. The western end of Marathon Valley is mapped as containing Fe-Mg smectite based
486 on analysis of multiple CRISM images of the region, with a (Fe,Mg)-OH 2.29 μm band depth
487 comparable to those from Mawrth Vallis (Fox et al., 2016). This signal encompasses most of the
488 western valley floor, including most of the lower-1 and lower-2 APXS targets. During
489 operations, a lower-1 outcrop containing the York and Jean Baptiste Deschamps targets was
490 modeled to be a locus of the strongest smectite signal and these two targets are separated as
491 representing a “smectite region” (Table 1). The analyses of these targets are clearly
492 distinguishable from those of other lower-1 targets in the AHCA modeling. The smectite region
493 analyses are the sole members of cluster 9 in major cluster B, while all other analyses of lower-1
494 targets are in major cluster C (Table 4a). Thus, the smectite region analyses are separated from
495 the other lower-1 analyses at the B-C separation at the third most dissimilar linkage (Fig. 8).

496 The smectite region rocks are less distinct from other lower-1 targets when the mobile
497 elements are excluded from the AHCA modeling. In this case, the smectite region analyses still
498 occur in a single cluster, but that cluster does include two other lower-1 analyses (Table 4b).
499 Furthermore, 89% of lower-1 analyses are in major cluster II along with the smectite region
500 analyses. This indicates that the smectite region rocks are not especially different in lithic
501 components, but rather, their distinction is more closely tied to the alteration that engendered
502 smectite formation.

503 4.3 Si-rich Lithic Types and pre-Endeavour Alteration

504 There are four silica-rich lithic types along Endeavour crater rim: (i) the Lihir/Espérance
505 boxwork veins that crosscut the Matijevic formation on Cape York (Arvidson et al., 2014; Clark
506 et al., 2016; Crumpler et al., 2015); (ii) the red-zone group from the Marathon Valley region; (iii)

purple erratic blocks first encountered on a ridge overlooking Marathon Valley; and (iv) pitted rocks from Perseverance Valley. These four rock types share the common characteristic of having higher SiO₂ and lower FeO than Shoemaker or Matijevic formation rocks (Fig. 6a), but for other elements, they can overlap the ranges for these formations and/or show distinct elemental trends between them (Fig. 6). All the boxwork vein analyses are in major cluster B, while all purple and pitted rock targets are in major cluster D (Table 4a; Fig. 8). The red-zone group analyses are distributed amongst major clusters A (27%), B (9%) and D (64%) (Table 4a). When the mobile elements are excluded from the AHCA modeling, major cluster IV contains only silica-rich rocks, including all boxwork vein, purple rock and pitted rock, and 82% of the red-zone group targets (Table 4b).

4.3.1 Boxwork Veins in the Matijevic Formation

The two abraded interiors of the boxwork veins have the highest SiO₂ and Al₂O₃ (Fig. 6c), the lowest FeO, MgO and CaO (Figs. 6a, b, d) and show the cleanest compositional signal of the vein material (Clark et al., 2016). These two analyses have the highest SiO₂ and lowest FeO and CaO of any target analyzed on Meridiani Planum. The boxwork vein compositions are consistent with montmorillonite plus silica having been the dominant phases in the veins (Arvidson et al., 2014; Clark et al., 2016). These veins were formed from hydrothermal solutions that were circumneutral to mildly alkaline in pH (Clark et al., 2016; Mittlefehldt et al., 2018a).

4.3.2 Red-zone Group in Marathon Valley

Unique to the Marathon Valley region (online supplement Fig. L06) are prominent curvilinear features crosscutting outcrop blocks containing rock with distinctive reddish color in Pancam false-color images (Fig. 10a) which we informally call “red zones.” At the head of Marathon Valley is a shallow, ovoid depression ~25×35 m in size – Spirit of Saint Louis (Fig. 1d) – which is partly bounded by a ~10-20 cm wide zone containing red-zone rocks crosscutting Shoemaker lower-2. Some of the outcrop blocks near Spirit of Saint Louis also exhibit compositional similarities to the red zones. Red zones were found within Marathon Valley proper crosscutting both lower-1 and lower-2 subunits. After leaving Marathon Valley on a feature named Spirit Mound (online supplement Fig. L08), we discovered an outcrop of lower-1 subunit bedrock cut by a composite silica-CaSO₄ vein-like structure (Fig. 15b) which shows geochemical similarities to red-zone rocks. All these targets are referred to as the red-zone group. Red-zone features were not observed outside the region of Marathon Valley and immediate surroundings, nor in the upper Shoemaker subunit.

Excluding the vein on Spirit Mound, rocks in the cores of red zones consist of discontinuous cm-sized knobs of rock with a hackly, cemented appearance (Fig. 10c). Many of them appear indurated, with clasts and matrix only poorly distinguished. They are distinct from rocks on either side of the red zone which are texturally typical of the Shoemaker lower-1 or lower-2 breccias which they crosscut (Figs. 10b, d).

Red zone rocks have unique compositional characteristics (Fig. 6). Most analyses occupy cluster 18 within major cluster D (Table 4a). The only other analyses in cluster 18 are two on

546 lower-2 target Muffler II. The two red-zone analyses in cluster 3 are targets on Gasconade3 and
547 4, a red-zone group vein on Spirit Mound. The other two outliers are Thermopylae2 and Private
548 Pierre Cruzatte, which have higher Ni contents (as do Gasconade3 and 4) than the other red-zone
549 group analyses. When the mobile elements are removed from the AHCA analyses,
550 Thermopylae2 and Private Pierre Cruzatte cluster with the other red-zone group analyses, while
551 Gasconade3 and 4 remain separated at the cluster level (Table 4b). Like the boxwork veins, the
552 red-zone group has higher SiO₂ and lower FeO contents compared to Shoemaker fm. breccias
553 (Fig. 6a). Furthermore, red-zone-group compositions follow the MgO-SiO₂ and CaO-SiO₂ trends
554 of the boxwork veins (Figs. 6b, d). One distinction between these two rock types is that the
555 boxwork veins show strong enrichments in Al₂O₃, while the red-zone rocks show more modest
556 enrichments, resulting in distinct Al₂O₃-SiO₂ trends (Fig. 6c). The red-zone group has Al₂O₃,
557 TiO₂ and Cr₂O₃ contents within ranges of Shoemaker lower-1 and lower-2 breccias (Figs. 6c, e,
558 f).

559 For the red zone around Spirit of Saint Louis we did three analyses each of red-zone
560 rocks and the host rock on either side of the red zone (Fig. 10a). Compared only to these adjacent
561 breccias, the red-zone rocks have enrichments in Al, Si, Ti, Cr and Ge (Fig. 11a). Potassium
562 contents are also higher than those of the nearby breccias but overlap the uncertainty envelope of
563 the mean host rock. Phosphorus, Ca and Zn overlap the composition of the mean host rock, while
564 the other elements are depleted relative to it. Considering only the red-zone target with the
565 highest SiO₂ content, Private William Bratton (Fig. 11a inset), Al, Si and Cr are well-resolved
566 from the host rock, while the uncertainties on K and Ti overlap the uncertainty envelope on the
567 host rock composition. Some bedrock blocks near the Spirit of Saint Louis feature have higher
568 Al₂O₃ and SiO₂ contents indicating red-zone-style alteration extended beyond the narrow,
569 visually defined red zones. Rocks on either side of the red zone and patches within it have
570 Pancam spectra which more closely resemble that of red hematite, indicating the presence of
571 crystalline ferric oxides within these rocks (Farrand et al., 2016).

572 Some rocks from the Spirit of Saint Louis region have elevated Ge contents. The highest
573 Ge contents are observed for red-zone-group rocks (Table 5). Germanium concentrations for
574 Private William Bratton from the red zone proper (853 µg/g) and Thermopylae2 from a nearby
575 outcrop block that has red-zone-group compositional characteristics (855 µg/g) are the highest
576 concentrations measured on Mars (cf., ~650 µg/g in the Garden City vein cluster crosscutting
577 Murray formation sandstones in Gale crater; Berger et al., 2017).

578 Germanium is mobilized in hydrothermal fluids, and hydrothermally altered seafloor
579 basalts on Earth show modest enrichments of a few µg/g in Ge (e.g., Escoube et al., 2015). In
580 terrestrial hydrothermal deposits, Ge substitutes in Fe-oxyhydroxides, sulfides or sulfosalts
581 (Bernstein, 1985). There is no correlation between Ge and either Fe or S for the rocks around
582 Spirit of Saint Louis, indicating that Fe-oxyhydroxides or S-bearing phases are not significant
583 hosts for Ge. At Gale crater, measurements made by the Curiosity rover APXS instrument show
584 that there is a broad positive correlation between Zn and Ge (Berger et al., 2017). In the Spirit of
585 Saint Louis region Zn and Ge are anti-correlated, indicating a different mechanism for Ge
586 enrichment than pertained at Gale crater.

587 Germanium concentrations in the region of Spirit of Saint Louis are roughly correlated
588 with Al_2O_3 and SiO_2 (Fig. 11b). Tetravalent Ge and Si have similar chemical properties, and Ge
589 substitutes for Si in minerals (e.g., see He et al., 2019). Hence, Ge is most likely substituted in
590 the silica phase in the red zones. The highest Ge contents are $\sim 20\times$ the general background
591 values (Fig. 11a) indicating the Ge enrichment could not have resulted from passive
592 concentration as more soluble elements were leached away; Ge must have precipitated from
593 solutions. This in turn suggests that at least a portion of the silica is a precipitate. Alumina, Ti
594 and Cr are also concentrated in the red-zone rocks, and these elements can be conserved during
595 hydrothermal alteration. A possible scenario for the red-zone-group rocks in the vicinity of Spirit
596 of Saint Louis is fluxing of hydrothermal fluids through fractures and nearby porous bedrock in
597 the region which resulted in localized alteration and leaching of the more soluble elements at
598 high water/rock, followed by precipitation of Ge-bearing silica. Hydrothermal solutions in
599 equilibrium with Ge-bearing silicates have higher Si and Ge concentrations and Ge/Si ratios at
600 higher temperatures (Pokrovski & Schott, 1998). Thus, simple cooling of solutions during
601 waning stages of hydrothermal activity could result in precipitation of Ge-rich silica.

602 The rocks in the Spirit of Saint Louis region show enrichments in Ge, but other bedrock
603 and red-zone-group targets from the Marathon Valley region do not have detectable Ge
604 (detection limit roughly 30 $\mu\text{g/g}$, but dependent on target composition and analytical conditions)
605 (Fig. 11b). This might suggest that there were differences in fluid compositions and/or properties
606 (temperature, pH, etc.) at this location. However, red-zone rocks with identical enrichments in
607 Al_2O_3 and SiO_2 and depletions in FeO have Ge contents that differ by a factor 30 or more (Fig.
608 11b). Any differences in fluid compositions and/or properties would have to be such that the
609 major elements were not affected. For example, fluid composition could have been affected by
610 earlier mineral precipitation, and in terrestrial systems, the Ge/Si of fluids can be increased by
611 this process (Escoube et al., 2015; Mortlock et al., 1993). This is unlikely to explain high- and
612 low-Ge red-zone rocks with similar SiO_2 contents as early precipitation of silica is commonly
613 invoked to explain such fluids (Escoube et al., 2015; Mortlock et al., 1993). An alternate
614 hypothesis is that the bedrock below Spirit of Saint Louis is atypically rich in Ge, but this merely
615 pushes the cause of Ge enrichment beyond our ability to test. With the observations at hand, we
616 cannot come to firm conclusions regarding the difference in Ge geochemistry in the lower
617 Shoemaker formation units in the Marathon Valley region.

618 4.3.3 Purple Rocks in the Marathon Valley Region

619 Purple rocks are erratic boulders scattered on a ridge overlooking the northeast side of
620 Marathon Valley and on the valley floor at the base of the ridge. They are identified by unique
621 purplish color in Pancam false-color composites (753, 535 and 432 nm) and a fine-grained,
622 almost aphanitic texture. The five analyses of this lithic type represent three different rocks.
623 Their silica contents are only marginally greater than those of Shoemaker formation breccias, but
624 their Al_2O_3 contents are much higher (Fig. 6c); two analyses of target Sergeant Nathaniel Pryor
625 are the highest Al_2O_3 contents measured on Meridiani Planum. Compared to the boxwork veins
626 and red-zone group, the purple rocks have very low MgO and Cr_2O_3 , Ni below the detection

627 limit, and widely varying TiO_2 (Table 1, Figs. 6b, e, f). These elemental distributions are very
628 different from the alteration signatures exhibited by the boxwork veins and red-zone group.

629 The silica- and alumina-rich compositions of the purple rocks could represent evolved
630 igneous compositions, but the case is not clear. On a total alkalis-silica diagram often used to
631 classify martian igneous rocks, they fall in the field of basaltic andesite. Igneous fractionation
632 from basaltic to intermediate compositions show generally increasing Al_2O_3 with SiO_2 , and
633 decreasing MgO , CaO , Cr_2O_3 and Ni (for example, the tholeiite to icelandite series at the
634 Torfajökull volcanic complex, Macdonald et al., 1990). Dark-rock boulder-float and rocks from
635 Wdowiak Ridge are potential pre-Endeavour basaltic rocks (Mittlefehldt et al., 2018a), and the
636 blue rocks are basaltic in composition. Elemental trends between these rock types and the purple
637 rocks (Fig. 6) are consistent with an igneous fractionation sequence. However, the wide range in
638 TiO_2 contents with little change in MgO or Cr_2O_3 is inconsistent with simple igneous
639 fractionation; a strong anticorrelation would be expected.

640 4.3.4 Pitted Rocks in Perseverance Valley

641 We encountered deeply pitted rocks in a linear outcrop in the central portion of
642 Perseverance Valley. These rocks, referred to here as pitted rocks, are thought to occupy a
643 fracture zone, possibly a fault trace, within the valley (Crumpler et al., 2020). They have a fine-
644 grained granular texture, lack visible clasts and contain mm-sized pits of uncertain origin (Tait et
645 al., 2019). Dark, fine-grained granular material is present within some pits which appears to be
646 dark sand, but some pits contain orangish-red (in false color) fine-grained fillings texturally
647 reminiscent of zeolites filling vesicles in altered basalt. These fillings have deep 535 nm
648 absorption bands indicative of abundant nanophase ferric oxides. Other pits have light-toned
649 rims. Light-toned coatings or rinds on parts of some pitted rocks give spectral evidence of
650 alteration (Farrand et al., 2019; Tait et al., 2019).

651 The five analyses of pitted rocks represent two different rocks and show varied
652 compositions. The three analyses with the lowest SiO_2 (targets Allende and Nazas) are in cluster
653 19 along with the purple rocks (Table 4a). The other pitted rock analyses (target Tomé) are in
654 cluster 20. Target Nazas was centered on a pit filled with fine-grained, acicular crystals to
655 capture the composition of alteration material and yielded a silica content intermediate between
656 Allende and Tomé. The Tomé analyses have the highest SiO_2 contents of any target from
657 Marathon and Perseverance Valleys and rival the highest SiO_2 contents measured for the
658 boxwork veins in the Matijevic formation (Fig. 6). Unlike the boxwork veins, the pitted rocks do
659 not show a positive correlation between Al_2O_3 and SiO_2 (Fig. 6c).

660 The similarity between Allende and the purple rocks suggest that this pitted rock could be
661 an evolved magmatic composition. The low MgO , FeO and Cr_2O_3 contents (Figs. 6a, b, f) and Ni
662 below detection all support this. However, the morphology and location of the pitted rocks as a
663 linear feature in a probable fault trace are not that of volcanic unit. The formation mechanism for
664 these rocks is uncertain (see Tait et al., 2019). They could be pseudotachylite formed in the
665 fracture either by impact or tectonic processes (Reimold, 1995). Pseudotachylite is a cataclastic
666 rock but the pitted rocks to not appear to be. The pitted rocks are juxtaposed with dark basaltic

667 rock in the fracture zone (Crumpler et al., 2020) and clasts of dark basalt in the dark-melt matrix
668 might have been difficult to distinguish in the rover images. The silica-rich Tomé targets cannot
669 be more evolved magmatic compositions than Allende because there is no substantial depletion
670 in them of MgO, FeO and Cr₂O₃ compared to Allende. An alternative hypothesis is that Tomé is
671 an altered composition of rock that might initially have been like Allende.

672 **4.3.5 Evaluation of Alteration in Si-rich Rocks**

673 Chemical alteration diagrams are used to document compositional changes in terrestrial
674 rocks caused by alteration and weathering. Figure 12a is a portion of an Al₂O₃,
675 (CaO*+Na₂O+K₂O), and (FeO_T+MgO) (A-CNk-FM) diagram (Nesbit & Wilson, 1992), and
676 Fig. 12b is a portion of a modified weathering intensity scale (WIS) diagram (Meunier et al.,
677 2013). These diagrams were devised to evaluate compositional changes occurring in rock during
678 soil formation. In the A-CNk-FM diagram, CaO* is measured CaO minus that contained in
679 apatite and carbonate (Nesbit & Wilson, 1992). We assumed all P₂O₅ is in apatite and had to
680 ignore calcite because CO₂ is not determined by the APXS. In the modified WIS diagram we
681 treat all iron as FeO because we have no measure of the ferric/ferrous ratio for the rocks. In Fig.
682 12a, pristine basaltic to intermediate igneous rocks will plot between the feldspar-olivine join
683 and the field for pyroxenes, as is observed for martian mafic rocks (blue rocks from the
684 Endeavour crater rim, and Adirondack-, Backstay- and Algonquin-class rocks from Gusev
685 crater). On both diagrams, magmatic differentiation will cause rock compositions to move from
686 the field for mafic rocks in the general direction towards the purple rocks. This is illustrated by a
687 suite of tholeiites through icelandites from the Torfajökull volcanic complex (Macdonald et al.,
688 1990). Low-temperature alteration on Earth (pedogenesis) of a range of primary rocks drives
689 compositions into the Al₂O₃ side of Fig. 12a and away from the Na+K+2Ca apex of Fig. 12b, as
690 illustrated by alteration for Monaro basalts from New South Wales, Australia (curved arrows)
691 (Eggerton et al., 1987). On Mars, alteration under low water/rock, acidic conditions in which
692 olivine is preferentially dissolved with the R²⁺ cations leached away would change pristine
693 martian basalt compositions directly away from the MgO+FeO_T (+MnO) apexes (blue arrows)
694 (Hurowitz & McLennan, 2007).

695 The four silica-rich rock types from the Endeavour crater rim show differing trends on
696 the alteration diagrams resulting in differing interpretations. The clearest signature for alteration
697 is shown by the boxwork veins crosscutting the Matijevic formation. Compositions of the two
698 abraded targets fall near or within the field of terrestrial montmorillonites (Fig. 12) (Wolters et
699 al., 2009), consistent with the interpretation of Clark et al. (2016). Clark et al. (2016) calculated a
700 pure vein composition for the Espérance vein by removing the instrument response to a small
701 amount of veneer material that was in the APXS field of view. The resulting composition plots
702 well within the fields for montmorillonite in Fig. 12. these analyses by removing aFive analyses
703 by sister rover Spirit of rock Independence from Gusev crater are shown for comparison as this
704 rock is thought to contain an alteration component close in composition to montmorillonite
705 (Clark et al, 2007). The rock shows clear evidence for alteration, but the signature for
706 montmorillonite is not as clearly expressed as for the boxwork veins. The red-zone group shows
707 less dramatic evidence for alteration on these diagrams, however, tie lines joining the host rock

708 composition for Private William Bratton with that red-zone target (white arrows) diverge from
709 vectors expected for alteration under low water/rock, acidic conditions (blue dashed arrows).
710 This, plus the arguments given in section 4.3.2 for coprecipitation of Si and Ge, indicates that
711 compositions of red-zone group rocks are not derived by simple passive enrichment as
712 ferromagnesian cations released by olivine dissolution are leached away.

713 The purple rocks show conflicting evidence regarding whether they are altered
714 compositions and if so, how they might have been altered. These rocks have compositions
715 broadly consistent with their being intermediate melts from a basalt fractionation sequence,
716 especially the two analyses of Bashful II which have the lowest Al_2O_3 contents (Fig. 6c). The
717 two purple rock analyses with highest Al_2O_3 (Sergeant Nathaniel Pryor) have CIPW norms that
718 are marginally corundum normative (one is; one is not). Corundum-normative compositions
719 indicate rock compositions that have been significantly altered from those of pristine magmatic
720 rocks (see discussions in Ming et al., 2006; Mittlefehldt et al., 2019b). The textures of purple
721 rocks are consistent with a fine-grained, quenched melt. Taken together, the evidence suggests
722 the purple rocks are slightly altered intermediate magmatic rocks. However, we cannot rule out
723 an origin as fragments of impact melt of slightly altered target rock with a mixed composition
724 like that of intermediate magmatic rocks. The purple rocks do not contain clasts which
725 commonly occur in impact melts, but this does not preclude an impact-melt origin. Observations
726 of flow features in impact-melt deposits in lunar craters indicate relatively fluid flow for
727 extended periods after the impact event for some (Bray et al., 2010). The morphology of some
728 impact-melt deposits indicates low viscosities, and therefore, low clast contents (Bray et al.,
729 2010; Stopar et al., 2014). Thus, an origin as fragments of an old ponded impact-melt sheet
730 remains viable for the purple rocks.

731 The pitted rock Allende mimics the purple rocks on the alteration diagrams, while the
732 Nazas and two Tomé targets show clear evidence of the effects of alteration. The Allende
733 analyses are fully consistent with a pristine intermediate magmatic composition. It is not
734 corundum normative, and, ignoring the ubiquitous SO_3 , Cl and Br, shows no compositional
735 evidence for alteration. As is the case for the purple rocks, an impact melt origin is viable,
736 specifically as pseudotachylite. The Nazas analysis was targeted on a pit largely filled with
737 reddish orange (in false color) acicular alteration material (Fig. 13), and its composition has
738 excess Al and a deficit in $\text{Na}+\text{K}+2\text{Ca}$ compared to the Bashful II analyses. These characteristics
739 and the texture are consistent with formation as a pit filling formed through alteration under
740 relatively high water/rock. Tomé is marginally on the Al-rich side of the feldspar-olivine join in
741 Fig. 12a and plots with Nazas on Fig. 12b, indicating an altered composition, consistent with
742 Pancam spectral evidence (Farrand et al., 2019; Tait et al., 2019).

743 **4.4 Sulfate-rich Rocks and Post-Endeavour Alteration**

744 We have previously documented episodes of sulfate-dominated alteration at several
745 locations along the Endeavour crater rim hosted in the Matijevic, Shoemaker (upper) and
746 Grasberg formations (Arvidson et al., 2014, 2016; Crumpler et al., 2015; Mittlefehldt et al.,
747 2018a; Squyres et al., 2012). Except for alteration in the Cook Haven region (Arvidson et al.,
748 2016), the sulfates are dominantly CaSO_4 in crosscutting veins (Fig. 14a). Relatively coarse

749 CaSO₄ veins occur in upper Shoemaker outcrops on Cape Tribulation (Mittlefehldt et al., 2018a)
750 and in the Grasberg formation which drapes over the lower reaches of the upper Shoemaker
751 (Crumpler et al., 2015; Squyres et al., 2012). These observations document a period of CaSO₄
752 precipitation from dilute solutions after formation of Endeavour crater and likely after deposition
753 of at least a portion of the Burns formation of sulfate-rich sandstones (Mittlefehldt et al., 2018a).
754 The thin CaSO₄ veins crosscutting the Matijevic formation (Arvidson et al., 2014) represent an
755 earlier, pre-Endeavour-impact period of sulfate precipitation, based on superposition
756 relationships. The veins are truncated by alteration veneers that were formed on an eroded
757 surface (unconformity) between the Matijevic and Shoemaker formations (Mittlefehldt et al.,
758 2018a).

759 In the Cook Haven region, sulfates were found as coatings on rock fragments overturned
760 by Opportunity's wheels; these are dominated by Mg-sulfates (Arvidson et al., 2016). Cook
761 Haven lies in a gentle depression on Murray Ridge where highly fractured outcrops are exposed.
762 The region is thought to be within a fracture zone transecting the Endeavour crater rim (Arvidson
763 et al., 2016). The rock coatings on Pinnacle Island and Stuart Island and the disturbed soil
764 Anchor Point show positive correlations between Mg and S, but not Ca and S (Figs. 14a, b).
765 These rock coatings include the highest measured SO₃ contents on Meridiani Planum. They are
766 also rich in MnO (Fig. 14c); Pinnacle and Stuart Islands have the highest MnO contents
767 measured on Meridiani Planum and Ni is positively correlated with MnO (Arvidson et al., 2016).
768 The high Mn contents are identified from Pancam 13-filter spectra as arising from one or more
769 Mn oxides (Arvidson et al., 2016). Further, the rock coatings on Pinnacle Island have high P₂O₅
770 contents; the second and third highest on Meridiani Planum (Arvidson et al., 2016). The
771 compositions and mineralogies of the coatings reflect precipitation of phases from solutions
772 formed through alteration of basaltic composition protoliths (Arvidson et al., 2016).

773 A S-rich region associated with fractures through Shoemaker lower-1 bedrock was found
774 in Marathon Valley (Fig. 15a). The bedrock includes a red-zone-group vein adjacent to the S-rich
775 region. Regolith in the fractures shows some compositional similarities to the altered rocks and
776 soils at Cook Haven. The two soil targets E Cann and Joseph Field show a positive correlation
777 between Mg and S, but not between Ca and S (Fig. 14a, b), but unlike the Cook Haven rock
778 coatings, E Cann and Joseph Field do not show elevated MnO (Fig. 14c) or P₂O₅. The high MnO
779 content of rock coatings on Pinnacle and Stuart Islands is considered to have been caused by late
780 oxidation of solutions prompting precipitation of Mn oxides (Arvidson et al., 2016). The
781 compositional signature of E Cann and Joseph Field is consistent with a similar formation
782 mechanism as that of the Cook Haven rock coating, minus the oxidation/precipitation of Mn
783 oxides and P enrichment.

784 The similar colored targets in the vicinity of E Cann and Joseph Field had Pancam 13f
785 spectra with a shallow absorption band centered between 803 and 864 nm (the Pancam R3 and
786 R4 bands). This absorption was comparable, albeit weaker in depth, and with a steeper blue to
787 red slope and concomitant diminishment of reflectance in the 673 nm (L3) band, as those
788 observed in spectra associated with light-toned, disturbed, sulfur-rich soils observed by the Spirit
789 rover in the Columbia Hills of Gusev crater (Fig. 16) (Farrand et al., 2016; Johnson et al., 2007).

790 Opportunity traveled eastward after leaving Marathon Valley towards the interior of
791 Endeavour crater to investigate the small knob Spirit Mound which we thought might expose
792 Matijevic formation outcrops. Mapping showed that bedrock at Spirit Mound was Shoemaker
793 lower-1 (Crumpler et al., 2020) that included a bright-vein-complex named Gasconade (Fig.
794 15b). We did two APXS measurements each of the vein interior and edge (Fig. 15c). The edge
795 samples, Gasconade3 and Gasconade4, clustered with the red-zone group in our early AHCA
796 modeling and we include them with this group here. However, although these targets are Si-rich
797 like the red-zone group, they are Al-poor compared to that group (Fig. 6c). The limited data on
798 hand do not allow us to determine the mechanism of SiO_2 enrichment. Because the Si-rich
799 sample is hosted in pre-Endeavour bedrock and has compositional signatures most similar to
800 other altered rocks that are pre-Endeavour, we interpret this as a pre-Endeavour alteration. The
801 interior samples are sulfate-rich, and tie lines between the silica-rich and sulfate-rich samples
802 indicate CaSO_4 dominates (Fig. 14 a, b). As discussed above, CaSO_4 veins are common in post-
803 Endeavour rocks suggesting that Gasconade and 2 might have been precipitated much later from
804 solutions following an older vein system. However, CaSO_4 veins are also present in the
805 Matijevic formation and are pre-Endeavour. Thus, the timing of formation of the Gasconade
806 CaSO_4 veins relative to the Endeavour impact is indeterminant.

807 The results of compositional measurements of alteration materials along the crater rim
808 demonstrate that alteration in the pre-Endeavour basement commonly resulted in precipitation of
809 silica \pm alumina with some CaSO_4 precipitation, and that this reflects alteration by circumneutral
810 solutions (Clark et al., 2016). In contrast, post-Endeavour alteration was dominantly a sulfate-
811 forming process. We suggest that the Mg-sulfate alteration observed at Cook Haven and
812 Marathon Valley likely was a response to hydrothermal solutions flowing through fractures in
813 the bedrock closely associated in time with the impact event. The crosscutting CaSO_4 veins in
814 upper Shoemaker and Grasberg formations represent a much later episode of sulfate precipitation
815 that occurred after Burns formation sulfate-sands were being deposited at Meridiani Planum
816 (Mittlefehldt et al., 2018a).

817 **4.5 Surface vs. Interior Composition**

818 We have investigated five Shoemaker formation targets where we analyzed untreated,
819 brushed and abraded targets to get information on compositions of the interiors, possible
820 coatings, and differences in composition between interiors and brushed surfaces to evaluate
821 possible surface-alteration zones: Private Robert Frazer; Pierre Pinaut; Private John Potts; Aguas
822 Calientes; and Salisbury. Private Robert Frazer is from an outcrop situated on the northern side
823 of Marathon Valley, east of a short ridge that forms part of the northern wall of the valley, while
824 Pierre Pinaut is from an outcrop near the southern margin of Marathon Valley, approximately 50
825 m southwest of Private Robert Frazer. These targets are on outcrops of Shoemaker lower-1.
826 Private John Potts is from a Shoemaker lower-2 outcrop located along the southern margin of
827 Marathon Valley near Opportunity's egress point from the valley. It is about 60 m due east of
828 Private Robert Frazer and ~90 m northeast of Pierre Pinaut. Aguas Calientes is from a lower
829 Shoemaker outcrop block situated in the middle of Perseverance Valley roughly at the furthest
830 point into the valley explored by Opportunity. Salisbury is from the Chester Lake member of the

831 Shoemaker formation located on the southeastern end of Cape York. This outcrop was discussed
832 by Squyres et al. (2012) where it was referred to as Chester Lake.

833 We normalized interior compositions to the cleanest brushed surface compositions for
834 each target, and to the extent possible, compare brushed with interior compositions taken at
835 identical APXS coordinates. Two abrasion activities were done on each of the rocks. We discuss
836 the results for each abrasion for Private John Potts, Aguas Calientes and Salisbury. For Private
837 Robert Frazer, the initial grind resulted in a partial abrasion circle, and APXS analyses on the
838 brushed surface were not co-located with the post-abrasion spot. The analysis after the initial
839 abrasion is not discussed. For Pierre Pinaut, the first grinding operation on did not significantly
840 abrade the surface. The APXS results after the first abrasion were considered the cleanest surface
841 analysis and used for normalizations for this target. The analysis campaigns resulted in eight
842 interior-exterior pairs for the various lower Shoemaker targets, and two for Salisbury.

843 A qualitative synopsis of the interior/exterior results is given in Table 6 where a 3σ
844 uncertainty level is used to identify elements in interior compositions that are greater than, less
845 than, or equal to the brushed surface analyses. Silica is the most abundant element in Shoemaker
846 formation breccias, and variations in Si within the suite are relatively small. At the 3σ level, Si
847 mass-ratios are greater in the interiors than the exteriors in about half the targets, and equal to
848 them in the other half. The closure restraint on major element analyses can cause false
849 correlations (Chayes, 1971). To avoid false conclusions, we have evaluated only Si-normalized
850 mole-ratios.

851 Quantitative comparisons of interiors to exteriors using Si-normalized mole-ratios
852 (hereafter, ratios) show several commonalities among the lower Shoemaker breccias (Fig. 17a).
853 Magnesium ratios are greater in all ten interiors, while Ca and Cl are lower in all, demonstrating
854 unambiguous evidence for systematic compositional differences between interiors and cleaned
855 surfaces. Sulfur ratios are lower in the Pierre Pinaut and Aguas Calientes targets except for one
856 of the three Pierre Pinaut targets where it is slightly lower but within 3σ of the brushed analysis.
857 Sulfur ratios are higher in Robert Frazer and Private John Potts interiors. The Br ratios (not
858 shown) of Private Robert Frazier and Aguas Calientes are higher in the interiors, but otherwise
859 are equivalent to the brushed targets within uncertainty. If we relax the confidence level to 2σ ,
860 Zn ratios are lower in the interiors of seven targets and are never higher in the interiors.

861 The common depletions in Ca and Cl in the interiors relative to brushed surfaces suggests
862 that these elements were mobilized out of the shallow interiors and onto surfaces. In general,
863 addition of Ca and Cl in a mole ratio of 1:2 to interior compositions can replicate the Ca/Si and
864 Cl/Si ratios of the brushed surfaces (Fig. 17b). Only small amounts of Ca-Cl salt would need to
865 be added; roughly 0.75-1.5 wt% if the salt is CaCl_2 , more if it is a perchlorate. The Private John
866 Potts and two of the Pierre Pinaut brushed surfaces have excess Ca over the simple model of Ca-
867 Cl-salt addition. Unfortunately, there is no definitive explanation for these three brushed surface
868 compositions, although mobilization of additional Ca salts could be the cause. The
869 interior/exterior differences support a scenario in which Ca salts, dominated by Cl-bearing salts,
870 have been wicked to the surfaces of rocks by small amounts of water.

871 The cause for higher Mg ratios in interiors is difficult to explain because there is no
872 measured anion that could suggest mobilization of specific Mg salts in all cases. The abraded
873 targets of Private Robert Frazer and Private John Potts have coupled enrichments of Mg and S,
874 and removal of MgSO₄ from the surface targets could explain the higher MgO contents of the
875 interior targets. For the other targets all measured anions excluding Br are lower in the interiors,
876 but Br is at too low a concentration to balance variations in Mg content. This implies that the
877 anion in a Mg salt is a light element not detected by the APXS, with carbonate being a plausible
878 candidate. Magnesium carbonate is detected elsewhere on Mars and is especially prevalent in
879 Nili Fossae where it is associated with olivine-rich units (e.g., Ehlmann et al., 2008; Niles et al.,
880 2013). Magnesium-rich carbonate formation occurs during alteration of olivine to serpentine
881 (e.g., Brown et al., 2010; Viviano et al., 2013). Magnesium-rich carbonate was detected by sister
882 rover Spirit in Gusev crater as an alteration phase in the Comanche Spur outcrop, but this
883 carbonate was calculated to contain a significant siderite component (Morris et al., 2010). There
884 is no systematic difference for Fe between interior and surface analyses and thus any carbonate
885 deposited in the interiors does not contain a significant siderite component.

886 The increase in Mg/Si in the interiors implies differential mobility of Mg relative to Si
887 but the mechanism cannot be uniquely determined. The increase in Mg/Si could indicate either
888 loss of Si from the surface or deposition of Mg just below the surface, but the latter is more
889 plausible. A possible scenario to explain the common Mg, Ca and Cl differences between
890 surfaces and ~1 mm depth in the Shoemaker breccias is as follows:

- 891 • Thin films of water periodically form on rock surfaces when atmospheric conditions
892 allow, which penetrate the interior by capillary action.
- 893 • Soluble alteration products within the rock are taken into solution.
- 894 • As water evaporates from the surface, the least soluble salts precipitate in voids in the
895 rock, gradually filling cracks.
- 896 • The most soluble salts, such as CaCl₂ or Ca(ClO₄)₂, are concentrated on the surface as
897 the last of the water evaporates.

898 The occurrence of a similar interior/surface compositional pattern for Shoemaker
899 formation breccias from Cape York, Marathon Valley and Perseverance Valley demonstrates that
900 it is a regional process that likely is relatively young. Rocks in Marathon and Perseverance
901 Valleys show “rock tails” – small aligned linear ridges of matrix material emanating from clasts
902 standing above the general outcrop surface – which are interpreted as abrasion shadows formed
903 as saltating sand planes down outcrop surfaces (e.g., Sullivan et al., 2005). The rock tails are
904 often several mm in width and of comparable height (Fig. 9). The amount of surface removed
905 from the outcrop is thus at least of the same order as the typical depth of abrasion (1-2 mm) and
906 indicates that formation of the Ca-Cl-rich crust is keeping pace with the abrasive removal of the
907 outcrop surface. Golombek et al. (2006) have estimated denudation rates on Meridiani Planum
908 during the Amazonian to be 10⁻² to 10⁻³ m/Myr. If this rate applies to Marathon and Perseverance
909 Valleys, then only 200,000 to 2,000,000 years is required to strip off 2 mm of rock surface.
910 Higher rates of erosion (by one to two orders of magnitude) are associated with the degradation
911 of small craters via sand abrasion and infill (Golombek et al., 2014), which would erode rock

912 tails in 2,000 to 20,000 years. Thus, a strong case can be made that the Ca-Cl-rich crusts are
913 being periodically renewed in very recent times.

914 **5. Marquette Island**

915 Marquette Island is an ~30×30 cm, wedge-shaped block standing on end on the hematite
916 plains roughly 11,800 meters from the Endeavour crater rim (Fig. 18a). The side of first
917 approach (front side) is dust covered, but the top is relatively dust free. We investigated brushed
918 and abraded targets on the front side and an untreated target on the top. The top surface shows an
919 irregular, granular morphology with lineations roughly parallel to the flat front side (Fig. 18b).
920 The MI image of the untreated top surface shows angular-blocky to rounded grains in a fine-
921 grained matrix (Fig. 18c). The MI image from the abrasion hole shows clasts of differing
922 brightness, some darker than the matrix, some brighter (Fig. 18d). The larger clast-supported
923 grains are poorly sorted, with no preferred orientation. There is no evidence for sedimentary
924 structures or layering. There are instances of what appear to be semi-arcuate structures (Fig.
925 18d), which suggests the rock may contain what might have been glassy shards; the semi-arcuate
926 structures are not common. The rock appears well lithified. Bright veins ~100 µm by ~2-3 mm
927 are present (Fig. 18c), suggesting localized alteration. Some regions show possible igneous
928 texture, confounding the textural interpretation of Marquette Island. The texture is not highly
929 diagnostic of a process or origin but is grossly like the target Seminole on the Columbia Hills in
930 Gusev crater. Yingst et al. (2007) considered Seminole to be part of a tephra sequence, while
931 Crumpler et al. (2011) also included impact ejecta and epiclastic origins as possible modes of
932 formation for clastic rocks on Columbia Hills, including Seminole.

933 The Mössbauer spectrometer was still active for the investigation of Marquette Island,
934 and two targets were investigated. Because the APXS compositions were very similar, the
935 Mössbauer data for the targets were combined and reduced as a single spectrum. The major iron-
936 bearing minerals are olivine (70% of the Fe), pyroxene (24%) and nanophase ferric oxide (6%).
937 This gives $\text{Fe}_{\text{oliv}}/(\text{Fe}_{\text{oliv}}+\text{Fe}_{\text{pyx}}) = 0.72$, and $\text{Fe}^{3+}/\Sigma_{\text{Fe}} = 0.06$. The nanophase ferric oxide is plausibly
938 contained in dust coatings, and there is no indication of Fe-bearing alteration phases. This is
939 consistent with results expected of a very fresh magmatic rock or a breccia composed of such
940 rocks.

941 Seven APXS measurements were made on Marquette Island, one on an untreated target
942 on the top side, two on brushed spots on the front side, and four analyses in an abrasion hole on
943 the front side; we concentrate here on the abraded targets. Marquette Island is compositionally
944 distinct from all other materials analyzed by Opportunity; all analyses are members of cluster 15
945 in the first AHCA model with only a single interloper of another rock type (Fig. 8; Table 4a), and
946 are the sole residents of cluster 13 when the mobile elements are excluded (Table 4b). Marquette
947 Island is lower in SiO_2 and TiO_2 , and higher in MgO and Cr_2O_3 than Shoemaker formation
948 breccias, the Matijevic formation or average Mars crust (Fig. 6). The closest compositional
949 match to Marquette Island among materials studied by the MER mission are Adirondack-class
950 basalts from Gusev crater but Marquette Island has higher MgO and lower CaO than those.

951 The APXS spectra of Marquette Island includes scatter peaks that can be used to

952 calculate excesses in light elements ($Z < 11$) in them compared to other samples of broadly
953 similar composition. For geological samples, H, O and C are the most likely light elements. The
954 scatter peaks arise from elastic (Rayleigh) and inelastic (Compton) scattering of Pu L_a X-rays
955 emitted from the ²⁴⁴Cm source. Rayleigh and Compton scattering cross sections have different Z
956 dependencies for the X-rays. The fitted Compton/Rayleigh intensity ratio can be compared to a
957 theoretically derived ratio based on measured oxide concentrations; if the two are identical, low
958 Z elements are not present at significant quantities (see Campbell et al., 2008). An additional
959 assumption is that the sample is homogeneous. The scatter peaks are sensitive to the overall
960 composition of the sample at greater depth than sampled by the APXS for major elements.
961 Therefore, a different composition at greater depth could cause differences in Compton/Rayleigh
962 ratios that mimic a composition with excesses in $Z < 11$ elements.

963 The Compton/Rayleigh scatter peak ratio for individual Marquette Island spectra are
964 compared to several spectra on basaltic rocks and soils that are closest in composition to
965 Marquette Island from Meridiani Planum and Gusev crater (Fig. 19). The mean ratio for the
966 Marquette Island spectra is well-resolved from that of the other basaltic composition targets. The
967 Compton/Rayleigh ratios from the four abraded targets are not significantly different from those
968 of the brushed and untreated targets indicating that an artifact of a heterogeneously layered
969 surface can be ruled out. The scatter-peak data indicate an excess of light elements equivalent to
970 ~15% excess oxygen in Marquette Island compared to other similar martian basaltic
971 compositions.

972 Of the plausible light elements, additional O alone can be ruled out because the
973 Mössbauer spectra show that the Fe₂O₃ content is negligible and there are no other multivalent
974 major elements that could be at higher oxidation state than normal. Hydrogen (OH⁻ and/or H₂O)
975 and CO₂ are possible candidates. (We exclude the possibility of abundant organic compounds or
976 elemental C.) The ~15 wt% equivalent oxygen translates to ~14 wt% OH⁻, ~13 wt% H₂O or ~5.5
977 wt% CO₂. We cannot determine which phase(s) might be present, but any carbonate or H-bearing
978 phase cannot contain Mössbauer-detectable amounts of Fe. Regardless, despite the low ferric
979 iron content that argues for a pristine rock, Marquette Island is either altered, or composed of
980 near-pristine igneous clastic materials cemented by volatile-bearing phases such as magnesite,
981 calcite, kieserite, etc. Marquette Island might be like Peace from Gusev crater: a clastic rock
982 bound by a cementing agent (Squyres et al., 2006b). Peace was the weakest rock abraded in
983 Gusev crater based on the specific grind energies calculated from the abrasion activity (1.4
984 J/mm³ vs. 2.5-44.8 for other rocks, Thomson et al., 2013), and is much lower than the value for
985 Marquette Island (11.5 J/mm³). Peace is posited to be comprised of basaltic grains cemented by
986 Mg- and Ca-sulfates (Ming et al., 2006). The greater strength and low-Z element content of
987 Marquette Island indicates that this rock is plausibly a carbonate-cemented clastic rock of
988 basaltic sand.

989 We conclude that Marquette Island is an ejecta block lying on the Burns formation
990 indicating that the source crater for it is penecontemporaneous with, or postdates, deposition of
991 the Burns sulfate sandstones. (If the former is correct, then Marquette Island is a lag boulder that
992 was exhumed from the Burns formation.) Two nearby craters penetrate the Burns formation and
993 excavated the underlying Noachian units. Iazu Crater is 6.8 km in diameter and located roughly

994 25 km south of Endeavour crater, and exposes a section of Burns formation overlying a lower
995 section of altered basaltic composition crust (Powell et al., 2017). Bopolu Crater is 19 km in
996 diameter and situated roughly 65 km southwest of Endeavour crater, and exposes a section of
997 Meridiani plains rocks above the Noachian basement (Grant et al., 2016). Marquette Island
998 plausibly is a fragment of the Noachian basement from one of these craters.

999 **6. Nature of the Subdued Cratered Unit**

1000 The geologic map of Meridiani Planum by Hynek and Di Achille (2017) shows an
1001 expanse of the Noachian subdued cratered unit 35-55 km south of the region explored by
1002 Opportunity (Fig. 2). They interpret this unit to be composed of volcanic deposits including lava
1003 and pyroclastic flows, impact breccias, impact-melt sheets, and erosional deposits formed via
1004 fluvio-lacustrine and aeolian processes. The area immediately surrounding Opportunity for
1005 several tens to a hundred km or more in every direction is the Hesperian hematite unit (Hynek &
1006 Di Achille, 2017), which Opportunity observations show is a hematite-spherule lag deposit plus
1007 aeolian ripples that is from a few cm up to about a meter thick (Soderblom et al., 2004; Sullivan
1008 et al., 2005). The hematite spherules are weathered out of the Burns formation and thus it is
1009 probable that this formation immediately underlies the hematite unit everywhere within the map
1010 region (Fig. 2).

1011 The Noachian/Hesperian Meridiani upper etched unit directly overlies the subdued
1012 cratered unit or the Noachian cratered unit along most of its southern, eastern and northern
1013 exposures (Fig. 2) (Hynek & Di Achille, 2017). This implies that the lower and middle Meridiani
1014 etched plains units could be absent at the Opportunity field site. Hynek and Di Achille (2017)
1015 concluded that the upper etched unit was formed as aeolian and/or volcanic deposits that were
1016 cemented by groundwater activity. The upper most few meters of this unit consists of the Burns
1017 formation, which is mostly sulfate-rich sandstones with a small amount of mudstone (Edgar et
1018 al., 2012; Grotzinger et al., 2005). The sandstones are mostly aeolian in origin, but some facies
1019 indicate localized fluvial reworking and deposition in a lacustrine setting is possible for some
1020 (Edgar et al., 2012, 2014; Grotzinger et al., 2005, 2006; Hayes et al., 2011). The fact that the
1021 hematite unit is absent over the Meridiani upper etched unit west, north and east of the area
1022 explored by Opportunity implies that classic Burns formation containing hematite concretions
1023 might not be present in these areas. This could be because the diagenetic processes that form the
1024 hematite spherules (McLennan et al., 2005) did not occur in those regions, because the Meridiani
1025 upper etched unit there is distinct from the Burns formation, or because the Burns formation and
1026 hematite unit have been eroded away.

1027 Supporting evidence that the Burns formation directly overlies the subdued cratered unit
1028 in the region explored by Opportunity comes from studies of Bopolu and Iazu Craters just south
1029 and southwest of Endeavour crater (Fig. 2). Bopolu Crater lies inside ancient Miyamoto crater
1030 and is younger than Endeavour crater; it postdates deposition and some erosional stripping of the
1031 Meridiani plains units that partially fill Miyamoto crater (Grant et al., 2016). The crater wall
1032 exposes a Noachian surface directly overlain by layered sulfates of the Meridiani plains (Grant et
1033 al., 2016). The Noachian surface represents the floor of Miyamoto crater at the time the layered
1034 sulfates were deposited. Iazu Crater lies closer to Endeavour crater and shows a similar

1035 stratigraphy in its walls. Layered, hydrated-sulfate- and hematite-bearing rocks – Burns
1036 formation – directly overlying basaltic composition rocks (spectral determinations of low- and high-
1037 Ca pyroxene) that contain smectite (Powell et al., 2017).

1038 The subdued cratered unit at Endeavour crater is represented by the Matijevic formation
1039 and the lower units of the Shoemaker formation. These were target rocks at the Endeavour
1040 impact site in the region of the western rim. The Matijevic formation is of uncertain origin
1041 because the limited exposure on Cape York and lack of diagnostic structures or textures did not
1042 allow for firm conclusions. This formation is composed of fine-grained clastic rocks that could
1043 be an air fall deposit of volcaniclastic or impact origin (Crumpler et al., 2015). In contrast, the
1044 lower units of the Shoemaker formation are polymict impact breccias based on textures, and the
1045 small clast size and low clast to matrix ratio indicates that they represent distal ejecta from one or
1046 more impacts. The pitted rocks and dark basaltic rocks in Perseverance Valley are also part of
1047 the pre-Endeavour basement. Because the pitted rocks are within a narrow fracture zone, their
1048 mode of formation cannot be determined (Tait et al., 2019). The dark rocks that cap Wdowiak
1049 Ridge are likely moderately altered volcanic rocks on an exposed, uplifted block of the pre-
1050 impact surface (Mittlefehldt et al., 2018a). Thus, ground observations by Opportunity are
1051 consistent with mapping from orbit on the types of materials that compose the subdued cratered
1052 unit and give a more detailed look at the origin of some components of the unit.

1053 Depending on the timing of the Endeavour impact, the upper Shoemaker may also be part
1054 of the subdued cratered unit. Grant et al. (2016) concluded that the Endeavour rim was degraded
1055 in part by fluvial processes and this is also indicated by modeling of Endeavour crater
1056 degradation (Hughes et al., 2019). Fluvial erosional and depositional processes were important in
1057 modifying subdued cratered unit surfaces, but not on the overlying Noachian cratered unit
1058 (Hynek & Di Achille, 2017).

1059 The very-fine-grained Grasberg formation is of uncertain stratigraphy. It is an airfall
1060 deposit that drapes the lower slopes of the eroded Endeavour rim (Crumpler et al., 2015) and
1061 thus likely postdates the period of fluvial erosion that degraded the Endeavour rim. It almost
1062 certainly predates deposition of the Burns formation at Endeavour crater (Crumpler et al., 2015;
1063 Mittlefehldt et al., 2018a). Crumpler et al. (2015) suggested that the Grasberg formation could be
1064 part of a widespread, possibly global, unit, and likened it to the Medusae Fossae Formation. How
1065 it might fit into the stratigraphy mapped by Hynek and Di Achille (2017) is unclear.

1066 7. Conclusions

1067 The Shoemaker formation stratigraphy, particularly well-exposed at Marathon Valley,
1068 shows two types polymict impact breccia. Upper units are clast-rich with coarser clasts, while
1069 lower units are clast-poor with smaller clasts (Crumpler et al., 2020). Studies of impact breccias
1070 at terrestrial craters show that vertical size-sorting is not present in ejecta deposits, but that
1071 sorting does occur with radial distance from crater rims, with more distal ejecta having a smaller
1072 average clast size, and a higher matrix content (Hörz et al., 1983; Oberbeck, 1975). The
1073 Shoemaker formation stratigraphy with clast-rich and clast-poor units is thus inconsistent with
1074 deposition as a single ejecta deposit from an impact. We conclude that the lower units are more

1075 distal ejecta from one or more earlier impacts, and the upper units are ejecta from Endeavour
1076 crater. The lower units, plus the Matijevic formation exposed on Cape York, represent part of the
1077 pre-Endeavour geology, which we equate with being subunits of the Noachian subdued cratered
1078 unit (Hynek & Di Achille, 2017). The lower Shoemaker units represent at least two depositions
1079 of distal impact ejecta and attest to the vibrancy of impact processes in the Noachian. The
1080 Matijevic formation, considered correlative with the lower Shoemaker units (Crumpler et al.,
1081 2020), could also be distal impact ejecta or it could be a volcanioclastic deposit (Crumpler et al.,
1082 2015). The Matijevic formation is compositionally distinct from the Shoemaker formation
1083 (Crumpler et al., 2015; Mittlefehldt et al., 2018a) and attests to the lithic diversity of the subdued
1084 crater unit.

1085 Statistical modeling of compositions sans volatile (S, Cl and Br) and mobile (P, Mn, Ni
1086 and Zn) elements show that the upper and lower subunits of the Shoemaker formation are for the
1087 most part indistinguishable. This indicates that lithic material like the lower Shoemaker
1088 formation is the major component of the upper Shoemaker. An exception is the Copper Cliff
1089 member on Cape York which contains a significant component of the underlying Matijevic
1090 formation. This indicates that a ballistic erosion-sedimentation process was important in
1091 deposition of the Copper Cliff member (Mittlefehldt et al., 2018a). Modeling that includes the
1092 mobile elements shows that Shoemaker formation rocks from Cape York can be distinguished
1093 from those on Cape Tribulation. This suggests general differences in style and/or degree of
1094 alteration between the two rim segments (cf., Mittlefehldt et al., 2018a).

1095 Unique to the pre-Endeavour rocks is alteration involving enrichments in Si and Al in
1096 vein-like structures that crosscut outcrops, and formation of smectite. Boxwork veins cutting the
1097 Matijevic formation were formed as mixtures of montmorillonite and silica produced by
1098 moderate-temperature alteration of bedrock by circumneutral to mildly alkaline fluids under high
1099 water/rock conditions (Clark et al., 2016). Red-zone group rocks form curvilinear traces cutting
1100 lower Shoemaker formation bedrock and are enriched in Si, Al, and sometimes Ge, compared to
1101 host bedrock. The Ge and at least some of the silica was formed by precipitation from
1102 hydrothermal fluids, indicating alteration under high water/rock. Ferric smectite was observed
1103 from orbit in a small region on Cape York and in Marathon Valley. The former is in dark veneers
1104 on Matijevic formation outcrops (Arvidson et al., 2014), while the latter is hosted in the lower-1
1105 and lower-2 units of the Shoemaker formation. Association of ferric smectite in the Noachian
1106 basement is also indicated by observations of smectite-bearing basaltic-composition rock in the
1107 walls of Iazu Crater (Powell et al., 2017) and the floor of Miyamoto crater (Wiseman et al.,
1108 2008).

1109 Post-Endeavour alteration is dominated by sulfate formation. Fracture zones in the crater
1110 rim include regions of alteration that produced Mg-sulfates as a dominant phase. This plausibly
1111 occurred as heated groundwaters circulated through the newly formed fractures and thus was
1112 closely associated in time with the impact (e.g., Arvidson et al., 2016), or could have occurred at
1113 some much later time, for example during the period of fluvial modification of the crater. Ca-
1114 sulfate vein formation also occurred, some pre-Endeavour and some much later. Coarse CaSO_4 -
1115 veins in the Grasberg formation and those in the upper Shoemaker formation near the current
1116 ridge crest were formed only after the Endeavour rim had been substantially degraded, and likely

1117 after deposition of the Burns formation (Arvidson et al., 2014; Crumpler et al., 2015; Mittlefehldt
1118 et al., 2018a). However, some Ca-sulfate veins were formed during pre-Endeavour times, as
1119 demonstrated by veins crosscutting the Matijevic formation (Arvidson et al., 2014; Crumpler et
1120 al., 2015; Mittlefehldt et al., 2018a). The Ca-sulfate component of the Gasconade composite vein
1121 might also be pre-Endeavour.

1122 Endeavour crater is Noachian in age, and thus, the upper Shoemaker unit might also be
1123 part of the subdued cratered unit. The degradation of Endeavour crater rim took place when
1124 surface waters were actively modifying surface morphology (Hughes et al., 2019), which is
1125 characteristic of the subdued crater unit (Hynek & Di Achille, 2017). However, the differences in
1126 alteration styles recorded in the upper Shoemaker vs. lower Shoemaker and Matijevic formation
1127 indicate that the former was deposited after a substantial time gap.

1128 Comparison of compositions of brushed rock surfaces and abraded interiors show
1129 systematic differences in Mg content and coupled differences in Ca and Cl that occur over depths
1130 as little as 1-2 mm. These are interpreted as arising from mobilization of near-surface salts by
1131 transient thin films of water followed by precipitation at different depths close to and on the
1132 surface. The rock surfaces are undergoing wind erosion as demonstrated by wind tails of mm-
1133 scale height formed behind erosion-resistant clasts. Estimates of erosion rates on Meridiani
1134 Planum indicate that 2 mm of outcrop surface can be removed within 2 million years; possibly
1135 much less than this (Golombek et al., 2006; 2014). Thus, Ca-Cl-salt deposition on surfaces must
1136 be renewed on this timescale, indicating that salt mobilization by transient water has occurred
1137 very recently, and could be ongoing.

1138 **Acknowledgements**-Rover operations described in this paper were conducted at the Jet
1139 Propulsion Laboratory, California Institute of Technology, under a contract with NASA. We
1140 thank the members of the MER project who enabled daily science observations at the
1141 Opportunity landing site. The senior author was supported by NASA through the Mars
1142 Exploration Rover Participating Scientist Program, and Planetary Science Research Programs.
1143 All data used in this article are listed in the references, tables, and supplements. [Data tables 1
1144 through 6 will be hosted in a data repository. We are currently seeking a host for the data.] Data
1145 for APXS integrations on all rock and soil targets acquired by Opportunity are available on the
1146 NASA Planetary Data System website: <http://pds-geosciences.wustl.edu/>.
1147

1148 **References**

- 1149 Aitchison, J. (1994). Principles of compositional data analysis. In: *Multivariate analysis and its*
1150 *applications*. Anderson, T. W., Fang, K. T., & Olkin, I. (eds.) Institute of Mathematical
1151 Statistics, Lecture Notes Monograph Series 24, Hayward, CA, 73-81.
- 1152 Andrews-Hanna, J. C., & Lewis, K. W. (2011). Early Mars hydrology: 2. Hydrological evolution
1153 in the Noachian and Hesperian epochs. *Journal of Geophysical Research: Planets*, 116(E2),
1154 E02007. doi:10.1029/2010JE003709
- 1155 Andrews-Hanna, J. C., Phillips, R. J., & Zuber, M. T. (2007). Meridiani Planum and the global
1156 hydrology of Mars. *Nature*, 446(7132), 163-166. doi:10.1038/nature05594
- 1157 Arvidson, R. E., Ashley, J. W., Bell, J. F., Chojnacki, M., Cohen, J., Economou, T. E., et al.
1158 (2011). Opportunity Mars Rover mission: Overview and selected results from Purgatory
1159 ripple to traverses to Endeavour crater. *Journal of Geophysical Research: Planets*, 116(E7),
1160 E00F15. doi:10.1029/2010JE003746
- 1161 Arvidson, R. E., Squyres, S. W., Bell, J. F., Catalano, J. G., Clark, B. C., Crumpler, L. S., et al.
1162 (2014). Ancient Aqueous Environments at Endeavour crater, Mars. *Science*, 343(6169).
1163 doi:10.1126/science.1248097
- 1164 Arvidson, R. E., Squyres, S. W., Morris, R. V., Knoll, A. H., Gellert, R., Clark, B. C., et al.
1165 (2016). High concentrations of manganese and sulfur in deposits on Murray Ridge,
1166 Endeavour crater, Mars. *American Mineralogist*, 101(6), 1389-1405. doi:10.2138/am-2016-
1167 5599
- 1168 Bell III, J. F., Squyres, S. W., Herkenhoff, K. E., Maki, J. N., Arneson, H. M., Brown, D., et al.
1169 (2003). Mars exploration rover Athena panoramic camera (Pancam) investigation. *Journal of*
1170 *Geophysical Research: Planets (1991–2012)*, 108(E12). doi:10.1029/2003JE002070
- 1171 Berger, J. A., Schmidt, M. E., Gellert, R., Boyd, N. I., Desouza, E. D., Flemming, R. L., et al.
1172 (2017). Zinc and germanium in the sedimentary rocks of Gale crater on Mars indicate
1173 hydrothermal enrichment followed by diagenetic fractionation. *Journal of Geophysical*
1174 *Research: Planets*, 122(8), 1747-1772.
- 1175 Bernstein, L. R. (1985). Germanium geochemistry and mineralogy. *Geochimica et*
1176 *Cosmochimica Acta*, 49(11), 2409-2422.
- 1177 Bray, V. J., Tornabene, L. L., Keszthelyi, L. P., McEwen, A. S., Hawke, B. R., Giguere, T. A., et
1178 al. (2010). New insight into lunar impact melt mobility from the LRO camera. *Geophysical*
1179 *Research Letters*, 37(21).
- 1180 Brown, A. J., Hook, S. J., Baldridge, A. M., Crowley, J. K., Bridges, N. T., Thomson, B. J., et al.
1181 (2010). Hydrothermal formation of clay-carbonate alteration assemblages in the Nili Fossae
1182 region of Mars. *Earth and Planetary Science Letters*, 297(1-2), 174-182.
- 1183 Cabrol, N. A., Herkenhoff, K., Knoll, A. H., Farmer, J., Arvidson, R., Grin, E., et al. (2014).
1184 Sands at Gusev crater, Mars. *Journal of Geophysical Research: Planets*, 119(5), 941-967.

- 1185 Campbell, J. L., Gellert, R., Lee, M., Mallett, C. L., Maxwell, J. A., & O'Meara, J. M. (2008).
1186 Quantitative in situ determination of hydration of bright high-sulfate Martian soils. *Journal*
1187 *of Geophysical Research: Planets*, 113(E6).
- 1188 Chayes, F. (1971). *Ratio correlation: a manual for students of petrology and geochemistry*. 99
1189 pp., University of Chicago Press, Chicago.
- 1190 Clark, B. C., Arvidson, R. E., Gellert, R., Morris, R. V., Ming, D. W., Richter, L., et al. (2007).
1191 Evidence for montmorillonite or its compositional equivalent in Columbia Hills, Mars.
1192 *Journal of Geophysical Research: Planets* 112, E06S01.
1193 <https://doi.org/10.1029/2006JE002756>
- 1194 Clark, B. C., Morris, R. V., Herkenhoff, K. E., Farrand, W. H., Gellert, R., Jolliff, B. L., et al.
1195 (2016). Esperance: Multiple episodes of aqueous alteration involving fracture fills and
1196 coatings at Matijevic Hill, Mars. *American Mineralogist*, 101(7), 1515-1526.
- 1197 Crumpler, L. S., Arvidson, R. E., Squyres, S. W., McCoy, T., Yingst, A., Ruff, S., et al. (2011).
1198 Field reconnaissance geologic mapping of the Columbia Hills, Mars, based on Mars
1199 Exploration Rover Spirit and MRO HiRISE observations. *Journal of Geophysical Research:*
1200 *Planets*, 116(E7).
- 1201 Crumpler, L. S., Arvidson, R. E., Bell, J., Clark, B. C., Cohen, B. A., Farrand, W. H., et al.
1202 (2015). Context of ancient aqueous environments on Mars from in situ geologic mapping at
1203 Endeavour crater. *Journal of Geophysical Research: Planets*, 120(3), 2014JE004699.
1204 doi:10.1002/2014JE004699
- 1205 Crumpler, L. S., Arvidson, R. E., Mittlefehldt, D. W., Grant, J. A., Farrand, W. H., & the Athena
1206 Science Team (2019). In Situ Mapping of the Structural and Stratigraphic Complexities of
1207 Endeavour crater's Rim. Paper presented at 50th Lunar and Planetary Science Conference,
1208 Abstract #1179, Houston, TX, USA.
- 1209 Crumpler, L. S., Arvidson, R. E., Mittlefehldt, D. W., Grant, J. A., & Farrand, W. H. (2020).
1210 Results from the first geologic traverse on the topographic rim of a complex impact crater,
1211 Endeavour Crater, Mars. *Geology*, 48(3), 252-257. (2020). <https://doi.org/10.1130/G46903.1>
- 1212 Edgar, L. A., J. P. Grotzinger, A. G. Hayes, D. M. Rubin, S. W. Squyres, J. F. Bell, et al. (2012).
1213 Stratigraphic architecture of bedrock reference section, Victoria crater, Meridiani Planum,
1214 Mars. *Sedimentary Geology of Mars, SEPM Special Publication*, 102, 195-209.
- 1215 Edgar, L. A., Grotzinger, J. P., Bell III, J. F., & Hurowitz, J. A. (2014). Hypotheses for the origin
1216 of fine-grained sedimentary rocks at Santa Maria crater, Meridiani Planum. *Icarus*, 234, 36-
1217 44.
- 1218 Eggleton, R. A., Foudoulis, C., & Varkevisser, D. (1987). Weathering of basalt: Changes in rock
1219 chemistry and mineralogy. *Clays and Clay Minerals*, 35(3), 161-169.
- 1220 Ehlmann, B. L., Mustard, J. F., Murchie, S. L., Poulet, F., Bishop, J. L., Brown, A. J., et al.
1221 (2008). Orbital identification of carbonate-bearing rocks on Mars. *Science*, 322(5909), 1828-
1222 1832.

- 1223 Escoube, R., Rouxel, O. J., Edwards, K., Glazer, B., & Donard, O. F. (2015). Coupled Ge/Si and
1224 Ge isotope ratios as geochemical tracers of seafloor hydrothermal systems: case studies at
1225 Loihi Seamount and East Pacific Rise 9°50' N. *Geochimica et Cosmochimica Acta*, 167, 93-
1226 112.
- 1227 Farrand, W. H., Johnson, J. R., Bell, J. F. III & Mittlefehldt, D. W. (2016). VNIR Multispectral
1228 Observations of Rocks at Spirit of St. Louis Crater and Marathon Valley on the Rim of
1229 Endeavour crater Made by the Opportunity Rover Pancam. Paper presented at 47th Lunar and
1230 Planetary Science Conference, Abstract #1983, Houston, TX, USA.
- 1231 Farrand, W. H., Johnson, J. R., Bell, J. F. III, Mittlefehldt, D. W., Schröder, C., Tait, A.,
1232 Arvidson, R. E. & Crumpler, L. C. (2019). Spectral Variability Among Rocks and Soils in
1233 Perseverance Valley, Mars as Observed by the Opportunity Pancam. Paper presented at 50th
1234 Lunar and Planetary Science Conference, Abstract #2403, Houston, TX, USA.
- 1235 Fox, V. K., Arvidson, R. E., Guinness, E. A., McLennan, S. M., Catalano, J. G., Murchie, S. L.,
1236 & Powell, K. E. (2016). Smectite deposits in Marathon Valley, Endeavour crater, Mars,
1237 identified using CRISM hyperspectral reflectance data. *Geophysical Research Letters*, 43,
1238 4885-4892. doi:10.1002/2016GL069108
- 1239 Gellert, R., Rieder, R., Brückner, J., Clark, B. C., Dreibus, G., Klingelhöfer, G., et al. (2006).
1240 Alpha Particle X-Ray Spectrometer (APXS): Results from Gusev crater and calibration
1241 report. *Journal of Geophysical Research: Planets*, 111(E2), E02S05.
1242 doi:10.1029/2005JE002555
- 1243 Golombek, M. P., Grant, J. A., Crumpler, L. S., Greeley, R., Arvidson, R. E., Bell III, J. F., et al.
1244 (2006). Erosion rates at the Mars Exploration Rover landing sites and long-term climate
1245 change on Mars. *Journal of Geophysical Research: Planets (1991–2012)*, 111(E12).
- 1246 Golombek, M. P., Warner, N. H., Ganti, V., Lamb, M. P., Parker, T. J., Fergason, R. L., &
1247 Sullivan, R. (2014). Small crater modification on Meridiani Planum and implications for
1248 erosion rates and climate change on Mars. *Journal of Geophysical Research: Planets*
1249 119(12), 2522-2547. doi:10.1002/2014JE004658
- 1250 Gorevan, S. P., Myrick, T., Davis, K., Chau, J. J., Bartlett, P., Mukherjee, S., et al. (2003). Rock
1251 abrasion tool: Mars exploration rover mission. *Journal of Geophysical Research: Planets
(1991–2012)*, 108(E12).
- 1253 Grant, J. A., Crumpler, L. S., Parker, T. J., Golombek, M. P., Wilson, S. A., & Mittlefehldt, D.
1254 W. (2015). Degradation of Endeavour crater, Mars. Paper presented at 46th Lunar and
1255 Planetary Science Conference, Abstract #2017, Houston, TX, USA.
- 1256 Grant, J. A., Parker, T. J., Crumpler, L. S., Wilson, S. A., Golombek, M. P., & Mittlefehldt, D.
1257 W. (2016). The degradational history of Endeavour crater, Mars. *Icarus*, 280, 22-36.
1258 doi:<http://dx.doi.org/10.1016/j.icarus.2015.08.019>
- 1259 Grotzinger, J. P., Arvidson, R. E., Bell III, J. F., Calvin, W., Clark, B. C., Fike, D. A., et al.
1260 (2005). Stratigraphy and sedimentology of a dry to wet eolian depositional system, Burns

- 1261 formation, Meridiani Planum, Mars. *Earth and Planetary Science Letters*, 240(1), 11-72.
1262 doi:<https://doi.org/10.1016/j.epsl.2005.09.039>
- 1263 Grotzinger, J., Bell III, J., Herkenhoff, K., Johnson, J., Knoll, A., McCartney, E., et al. (2006).
1264 Sedimentary textures formed by aqueous processes, Erebus crater, Meridiani Planum, Mars.
1265 *Geology*, 34(12), 1085-1088. doi:10.1130/g22985a.1
- 1266 Hayes, A. G., Grotzinger, J. P., Edgar, L. A., Squyres, S. W., Watters, W. A., & Sohl-Dickstein,
1267 J. (2011). Reconstruction of eolian bed forms and paleocurrents from cross-bedded strata at
1268 Victoria Crater, Meridiani Planum, Mars. *Journal of Geophysical Research: Planets*,
1269 116(E7).
- 1270 He, D., Lee, C. T. A., Yu, X., & Farner, M. (2019). Ge/Si partitioning in igneous systems:
1271 Constraints from laser ablation ICP-MS measurements on natural samples. *Geochemistry,*
1272 *Geophysics, Geosystems*, 20(10), 4472-4486.
- 1273 Herkenhoff, K. E., Squyres, S. W., Bell, J. F., Maki, J. N., Arneson, H. M., Bertelsen, P., et al.
1274 (2003). Athena Microscopic Imager investigation. *Journal of Geophysical Research: Planets*
1275 (1991–2012), 108(E12).
- 1276 Hötz, F., R. Ostertag, & D. A. Rainey (1983). Bunte Breccia of the Ries: Continuous deposits of
1277 large impact craters. *Reviews of Geophysics*, 21(8), 1667-1725.
1278 doi:10.1029/RG021i008p01667
- 1279 Hughes, M. N., Arvidson, R. E., Grant, J. A., Wilson, S. A., Howard, A. D., & Golombek, M. P.
1280 (2019). Degradation of Endeavour crater based on orbital and rover-based observations in
1281 combination with landscape evolution modeling. *Journal of Geophysical Research: Planets*,
1282 124(6), 1472-1494. doi:10.1029/2019je005949
- 1283 Hurowitz, J. A., & McLennan, S. M. (2007). A~ 3.5 Ga record of water-limited, acidic
1284 weathering conditions on Mars. *Earth and Planetary Science Letters*, 260(3-4), 432-443.
- 1285 Hynek, B. M., & Di Achille, G. (2017). *Geologic map of Meridiani Planum, Mars*. (Scientific
1286 Investigations Map 3356). Washington, DC: U.S. Geological Survey. <https://doi.org/10.3133/sim3356>
- 1288 Hynek, B. M., & Phillips, R. J. (2008). The stratigraphy of Meridiani Planum, Mars, and
1289 implications for the layered deposits' origin. *Earth and Planetary Science Letters*, 274(1–2),
1290 214-220. doi:<https://doi.org/10.1016/j.epsl.2008.07.025>
- 1291 Hynek, B. M., Arvidson, R. E. & Phillips, R. J. (2002). Geologic setting and origin of Terra
1292 Meridiani hematite deposit on Mars. *Journal of Geophysical Research: Planets*, 107(E10),
1293 5088, doi:10.1029/2002je001891
- 1294 Johnson, J. R., Bell III, J. F., Cloutis, E., Staid, M., Farrand, W. H., McCoy, T., et al. (2007).
1295 Mineralogic constraints on sulfur-rich soils from Pancam spectra at Gusev crater, Mars.
1296 *Geophysical Research Letters*, 34(13), L13202. doi:10.1029/2007GL029894
- 1297 Jolliff, B. L., Mittlefehldt, D. W., Farrand, W. H., Knoll, A. H., McLennan, S. M., & Gellert, R.
1298 (2019). Mars Exploration Rover Opportunity: Water and other volatiles on ancient Mars. In

- 1299 J. Filiberto, S. P. Schwenzer (Eds.), *Volatiles in the Martian Crust* (pp. 285-328).
1300 Amsterdam, Netherlands: Elsevier. doi:<https://doi.org/10.1016/B978-0-12-804191-8.00010-6>.
- 1302 Klingelhöfer, G., Morris, R. V., Bernhardt, B., Rodionov, D., de Souza Jr, P. A., Squyres, S. W.,
1303 et al. (2003). Athena MIMOS II Mössbauer spectrometer investigation. *Journal of*
1304 *Geophysical Research: Planets* (1991–2012), 108(E12). doi:10.1029/2003JE002138
- 1305 Macdonald, R., McGarvie, D. W., Pinkerton, H., Smith, R. L., & Palacz, A. (1990). Petrogenetic
1306 evolution of the Torfajökull Volcanic Complex, Iceland I. Relationship between the magma
1307 types. *Journal of Petrology*, 31(2), 429-459.
- 1308 Mader, M. M., & Osinski, G. R. (2018). Impactites of the Mistastin Lake impact structure:
1309 Insights into impact ejecta emplacement. *Meteoritics & Planetary Science*, 53(12), 2492-
1310 2518.
- 1311 Maki, J. N., Bell, J. F., Herkenhoff, K. E., Squyres, S. W., Kiely, A., Klimesh, M., et al. (2003).
1312 Mars Exploration Rover engineering cameras. *Journal of Geophysical Research: Planets*,
1313 108(E12).
- 1314 McLennan, S. M., Bell III, J. F., Calvin, W. M., Christensen, P. R., Clark, B. D., De Souza, P.
1315 A., et al. (2005). Provenance and diagenesis of the evaporite-bearing Burns formation,
1316 Meridiani Planum, Mars. *Earth and Planetary Science Letters*, 240(1), 95-121.
- 1317 Meunier, A., Caner, L., Hubert, F., El Albani, A., & Prêt, D. (2013). The weathering intensity
1318 scale (WIS): an alternative approach of the chemical index of alteration (CIA). *American*
1319 *Journal of Science*, 313(2), 113-143.
- 1320 Ming, D. W., Mittlefehldt, D. W., Morris, R. V., Golden, D. C., Gellert, R., Yen, A., et al.
1321 (2006). Geochemical and mineralogical indicators for aqueous processes in the Columbia
1322 Hills of Gusev Crater, Mars. *Journal of Geophysical Research: Planets* 111, E02S12. <https://doi.org/10.1029/2005JE002560>
- 1324 Mittlefehldt, D. W., Gellert, R., Herkenhoff, K. E., Morris, R. V., Clark, B. C., Cohen, B. A., et
1325 al. (2010). Marquette Island: A distinct mafic lithology discovered by Opportunity. Paper
1326 presented at 41st Lunar and Planetary Science Conference, Abstract #2109, Houston, TX,
1327 USA.
- 1328 Mittlefehldt, D. W., Gellert, R., Ming, D. W., Yen, A. S., Clark, B. C., Morris, R. V., et al.
1329 (2018a). Diverse lithologies and alteration events on the rim of Noachian-aged Endeavour
1330 crater, Meridiani Planum, Mars: In situ compositional evidence. *Journal of Geophysical*
1331 *Research: Planets*, 123(5), 1255-1306. doi:10.1002/2017JE005474
- 1332 Mittlefehldt, D. W., Crumpler, L. S., Grant, J. A., Arvidson, R. E., & Farrand W. H. (2018b).
1333 Noachian-aged pre-impact lithology exposed in Endeavour crater rim: Mars Exploration
1334 Rover Opportunity observations. Paper presented at 2018 Geological Society of America
1335 Annual Meeting.
- 1336 Mittlefehldt, D. W., Arvidson, R. E., Crumpler, L. S., Farrand, W. H., Gellert, R., Grant, J. A., et
1337 al. (2019a). Geochemistry of Noachian bedrock and alteration events, Endeavour crater,

- 1338 Mars. Paper presented at 50th Lunar and Planetary Science Conference, Abstract #1100,
1339 Houston, TX, USA.
- 1340 Mittlefehldt, D. W., R. Gellert, D. W. Ming, & A. S. Yen (2019b). Alteration processes in Gusev
1341 crater, Mars: Volatile/mobile element contents of rocks and soils determined by the Spirit
1342 Rover. In J. Filiberto, S. P. Schwenzer (Eds.), *Volatile in the Martian Crust* (pp. 329-368).
1343 Amsterdam, Netherlands: Elsevier. doi:<https://doi.org/10.1016/B978-0-12-804191-8.00011-8>
- 1344 Morris, R.V., Ruff, S.W., Gellert, R., Ming, D.W., Arvidson, R.E., Clark, B.C., et al. (2010).
1345 Identification of carbonate-rich outcrops on Mars by the Spirit rover. *Science*, 329(5990),
1346 421-424. doi:10.1126/science.1189667
- 1347 Mortlock, R. A., Froelich, P. N., Feely, R. A., Massoth, G. J., Butterfield, D. A., & Lupton, J. E.
1348 (1993). Silica and germanium in Pacific Ocean hydrothermal vents and plumes. *Earth and*
1349 *Planetary Science Letters*, 119(3), 365-378.
- 1350 Nesbitt, H. W., & Wilson, R. E. (1992). Recent chemical weathering of basalts. *American*
1351 *Journal of science*, 292(10), 740-777.
- 1352 Newsom, H. E., Barber, C. A., Hare, T. M., Schelble, R. T., Sutherland, V. A., & Feldman, W.
1353 C. (2003). Paleolakes and impact basins in southern Arabia Terra, including Meridiani
1354 Planum: Implications for the formation of hematite deposits on Mars. *Journal of Geophysical*
1355 *Research: Planets*, 108(E12). doi:10.1029/2002JE001993
- 1356 Newsom, H.E., Lanza, N.L., Ollila, A.M., Wiseman, S.M., Roush, T.L., Marzo, G.A., et al.
1357 (2010). Inverted channel deposits on the floor of Miyamoto crater, Mars. *Icarus*, 205(1), 64-
1358 72.
- 1359 Niles, P. B., Catling, D. C., Berger, G., Chassefière, E., Ehlmann, B. L., Michalski, J. R., et al.
1360 (2013). Geochemistry of carbonates on Mars: implications for climate history and nature of
1361 aqueous environments. *Space Science Reviews*, 174(1), 301-328.
- 1362 Oberbeck, V. R. (1975). The role of ballistic erosion and sedimentation in lunar stratigraphy.
1363 *Reviews of Geophysics*, 13(2), 337-362. doi:doi:10.1029/RG013i002p00337
- 1364 Parker, T. J., Golombek, M. P., Calef, F. J., & Hare, T. M. (2012). High-resolution basemaps for
1365 localization, mission planning, and geologic mapping at Meridiani Planum and Gale crater.
1366 Paper presented at 43rd Lunar and Planetary Science Conference, Abstract #2535, Houston,
1367 TX, USA.
- 1368 Pokrovski, G. S., & Schott, J. (1998). Thermodynamic properties of aqueous Ge (IV) hydroxide
1369 complexes from 25 to 350 C: implications for the behavior of germanium and the Ge/Si ratio
1370 in hydrothermal fluids. *Geochimica et Cosmochimica Acta*, 62(9), 1631-1642.
- 1371 Powell, K. E., Arvidson, R. E., Zanetti, M., Guinness, E. A., & Murchie, S. L. (2017). The
1372 structural, stratigraphic, and paleoenvironmental record exposed on the rim and walls of Iazu
1373 Crater, Mars. *Journal of Geophysical Research: Planets*, 122(5), 1138-1156.
- 1374 Reimold, W. U. (1995). Pseudotachylite in impact structures—generation by friction melting and
1375 shock brecciation?: A review and discussion. *Earth-Science Reviews*, 39(3-4), 247-265.

- 1376 Rieder, R., Gellert, R., Brückner, J., Klingelhöfer, G., Dreibus, G., Yen, A., & Squyres, S. W.
1377 (2003). The new Athena alpha particle X-ray spectrometer for the Mars Exploration Rovers,
1378 *Journal of Geophysical Research: Planets (1991–2012)*, 108(E12).
- 1379 Shoemaker, E. M. (1963). Impact mechanics at Meteor Crater, Arizona. In B. M. Middlehurst, G.
1380 P. Kuiper (Eds.), *The Moon, Meteorites and Comets*. (pp. 301-336). Chicago, IL, USA:
1381 University of Chicago Press.
- 1382 Soderblom, L. A., Anderson, R. C., Arvidson, R. E., Bell, J. F., Cabrol, N. A., Calvin, W., et al.
1383 (2004). Soils of Eagle crater and Meridiani Planum at the Opportunity rover landing site.
1384 *Science*, 306(5702), 1723-1726.
- 1385 Squyres, S. W., & Knoll, A. H. (2005). Sedimentary rocks at Meridiani Planum: Origin,
1386 diagenesis, and implications for life on Mars. *Earth and Planetary Science Letters*, 240(1), 1-
1387 10. doi:<https://doi.org/10.1016/j.epsl.2005.09.038>
- 1388 Squyres, S. W., Arvidson, R. E., Baumgartner, E. T., Bell, J. F., Christensen, P. R., Gorevan, S.,
1389 et al. (2003). Athena Mars rover science investigation. *Journal of Geophysical Research: Planets
1390 (1991–2012)*, 108(E12).
- 1391 Squyres, S. W., Arvidson, R. E., Bollen, D., Bell III, J. F., Brueckner, J., Cabrol, N. A., et al.
1392 (2006a). Overview of the *Opportunity* Mars Exploration Rover mission to Meridiani Planum:
1393 Eagle crater to Purgatory ripple. *Journal of Geophysical Research: Planets*, 111(E12),
1394 E12S12. doi:10.1029/2006je002771
- 1395 Squyres, S. W., Arvidson, R. E., Blaney, D. L., Clark, B. C., Crumpler, L., Farrand, W. H., et al.
1396 (2006b). Rocks of the Columbia hills. *Journal of Geophysical Research: Planets*, 111(E2).
- 1397 Squyres, S. W., Arvidson, R. E., Bell, J. F., Calef, F., Clark, B. C., Cohen, B. A., et al. (2012).
1398 Ancient impact and aqueous processes at Endeavour crater, Mars. *Science*, 336(6081), 570-
1399 576. doi:10.1126/science.1220476
- 1400 Stopar, J. D., Hawke, B. R., Robinson, M. S., Denevi, B. W., Giguere, T. A., & Koeber, S. D.
1401 (2014). Occurrence and mechanisms of impact melt emplacement at small lunar craters.
1402 *Icarus*, 243, 337-357.
- 1403 Sullivan, R., Banfield, D., Bell, J. F., Calvin, W., Fike, D., Golombek, M., et al. (2005). Aeolian
1404 processes at the Mars Exploration Rover Meridiani Planum landing site. *Nature*, 436(7047),
1405 58-61.
- 1406 Tait, A. W., Schröder, C., Farrand, W. H., Ashley, J. W., Cohen, B. A., Gellert, R., et al. (2019).
1407 Exploring origins of pitted/vesicular rocks in Perseverance Valley, Endeavour crater. Paper
1408 presented at 50th Lunar and Planetary Science Conference, Abstract #2327, Houston, TX,
1409 USA.
- 1410 Taylor, S. R., & McLennan, S. M. (2009). *Planetary Crusts: Their Composition, Origin and
1411 Evolution*. Cambridge, UK: Cambridge University Press.

- 1412 Thomson, B. J., Bridges, N. T., Cohen, J., Hurowitz, J. A., Lennon, A., Paulsen, G., & Zacny, K.
1413 (2013). Estimating rock compressive strength from Rock Abrasion Tool (RAT) grinds.
1414 *Journal of Geophysical Research: Planets*, 118(6), 1233-1244. doi:10.1002/jgre.20061
- 1415 Viviano, C. E., Moersch, J. E., & McSween, H. Y. (2013). Implications for early hydrothermal
1416 environments on Mars through the spectral evidence for carbonation and chloritization
1417 reactions in the Nili Fossae region. *Journal of Geophysical Research: Planets*, 118(9), 1858-
1418 1872.
- 1419 Wiseman, S. M., Arvidson, R. E., Andrews-Hanna, J. C., Clark, R. N., Lanza, N. L., Des
1420 Marais, D., et al. (2008). Phyllosilicate and sulfate-hematite deposits within Miyamoto crater
1421 in southern Sinus Meridiani, Mars. *Geophysical Research Letters*, 35(19), L19204.
1422 doi:10.1029/2008GL035363
- 1423 Wolters, F., Lagaly, G., Kahr, G., Nueeshch, R., & Emmerich, K. (2009). A comprehensive
1424 characterization of dioctahedral smectites. *Clays and Clay Minerals*, 57(1), 115-133.
- 1425 Wray, J. J., Noe Dobrea, E. Z., Arvidson, R. E., Wiseman, S. M., Squyres, S. W., McEwen, A.
1426 S., et al. (2009). Phyllosilicates and sulfates at Endeavour crater, Meridiani Planum, Mars.
1427 *Geophysical Research Letters*, 36(21), L21201. doi:10.1029/2009gl040734
- 1428 Yingst, R. A., Schmidt, M. E., Herkenhoff, K. E., Mittlefehldt, D. W., & the Athena Science
1429 Team (2007). Linking Home Plate and Algonquin class rocks through microtextural analysis:
1430 Evidence for hydrovolcanism in the inner basin of Columbia Hills, Gusev crater. Paper
1431 presented at 7th International Conference on Mars, Abstract #3296, Houston, TX, USA.
1432

- 1433 **Tables (in Excel file; to be hosted on data repository)**
- 1434 Table 1. APXS data table.
- 1435 Table 2. Average compositions of Shoemaker formation subunits.
- 1436 Table 3. Element/Si mole ratios and cluster membership for targets used in Agglomerative
- 1437 Hierarchical Cluster Analysis.
- 1438 Table 4a. Cluster hierarchy matrix from Agglomerative Hierarchical Cluster Analysis, excluding
- 1439 volatile elements (S, Cl, Br).
- 1440 Table 4b. Cluster hierarchy matrix from Agglomerative Hierarchical Cluster Analysis, excluding
- 1441 volatile elements and mobile elements (P, Mn, Ni, Zn).
- 1442 Table 5. Germanium concentrations for rocks in the Spirit of Saint Louis region.
- 1443 Table 6. Qualitative synopsis of interior/exterior ratios for Shoemaker formation rocks.
- 1444

1445 **Figure Captions**

1446 Figure 1. (a) High Resolution Imaging Science Experiment-based mosaic showing Endeavour
1447 crater. (b) Cape York. (c) The Cape Tribulation portion of the western rim showing the locations
1448 of Marathon and Perseverance Valleys. (d) Expanded view of Marathon Valley and Spirit of
1449 Saint Louis region. (e) Expanded view of Perseverance Valley region. Rover track shown in
1450 white. Images from HiRISE-based mosaic of Endeavour crater base map (Parker et al., 2012).

1451 Figure 2. Portions of the geological map of Meridiani Planum showing the relationships between
1452 the Noachian subdued cratered unit, the Noachian/Hesperian upper etched unit and the Hesperian
1453 hematite unit in the vicinity of the Opportunity traverse. The legend shows geologic units
1454 discussed here with the rover-based units identified. Modified from Hynek & Di Achille (2017).

1455 Figure 3. Pancam false-color images showing examples of macrotextures of Shoemaker
1456 formation outcrops: (a) Boesmanskop and Komati (clast), Greeley Haven member on Cape York
1457 (Sol 2795); (b) Moreton Island, upper Shoemaker formation on Murray Ridge, Cape Tribulation
1458 (Sol 3494); (c) Cape Elizabeth (outcrop block), upper Shoemaker, and Pinnacle Island (loose
1459 rock) in Cook Haven, Cape Tribulation (Sol 3540); (d) Thermopylae, lower-2 Shoemaker at
1460 Spirit of Saint Louis, Cape Tribulation (Sol 3998); (e) Smectite-rich outcrop, lower-1 Shoemaker
1461 in Marathon Valley (Sol 4419); (f) Mesilla, lower Shoemaker in Perseverance Valley (Sol 4880).
1462 False color rendered using Pancam left-eye filters 2, 5, and 7 centered on 753, 535, and 432 nm
1463 (hereafter L257). Scale bars are ~10 cm at the locations shown. The locations of these rocks can
1464 be found in online supplementary Figs. L02 through L04 and L09.

1465 Figure 4. Schematic diagram of ejecta emplacement outside a complex crater, after Oberbeck
1466 (1975). Insets show the area at the base of the ejecta curtain at three different times; solid arrows
1467 show schematic vectors of ejecta fragment motion; open arrows show schematic vectors of ejecta
1468 deposit motion. α - ejection angle; V – ejection velocity.

1469 Figure 5. Pancam false-color image (Gibraltar II panorama, L257) showing the contact between
1470 the upper and lower units of the Shoemaker formation in Marathon Valley. Images acquired
1471 between Sols 4446-4453. The location of this image can be found in online supplementary Fig.
1472 L07.

1473 Figure 6. Element vs. SiO₂ diagrams for Endeavour crater rim rocks, normalized to a SO₃-, Cl-
1474 and Br-free basis. Anomalous targets are Sledge Island and Sarcobatus Clast 2; see text. Labeled
1475 points in (c) are: A – Allende; G – Gasconade; N – Nazas; T – Tomé. Dotted field encloses the
1476 abraded targets of Marquette Island. White field labeled b is abraded targets of Adirondack-class
1477 basalts from Gusev crater. Locations of Allende, Nazas and Tomé (pitted rocks) can be found in
1478 online supplementary Fig. L10; that of Gasconade in Fig. L06; and those of Sledge Island and
1479 Sarcobatus Clast 2 in Fig. L03.

1480 Figure 7. Plot of SO₃ vs. Cl for Endeavour crater rim rocks.

1481 Figure 8. Dendrogram of Agglomerative Hierarchical Cluster Analysis (AHCA) of Endeavour
1482 crater rim rocks and soils. Inset shows expanded view of cluster 1; see text for explanation.

1483 Figure 9. Individual MI frames of Parral (Sol 4809), Waverly (Sol 4656) and Mesilla (Sol 4900)
1484 documenting the distinct texture of Parral compared to the upper Shoemaker target Waverly but
1485 like that of lower Shoemaker Mesilla. Clasts in Waverly (dark) are more abundant and up to 18
1486 mm in size, while those in Parral (heads of wind tails) are fewer and smaller (largest ~3 mm
1487 across). Images are 31 mm across. The location of Parral and Mesilla can be found in online
1488 supplementary Fig. L10; that of Waverly in Fig. L08.

1489 Figure 10. (a) Portion of a Pancam false-color mosaic (Sol 4033, L257) of red zone bordering
1490 north side of Spirit of Saint Louis with APXS/MI targets identified: B – Private William Bratton;
1491 C – Private Pierre Cruzatte; D – John Dame; R – Ryan NYP. (b) – (d) MI images of three of the
1492 APXS targets. Scale bar in (a) is ~25 cm at the location shown. MI images are 31 mm across.
1493 The location of these images can be found in online supplementary Fig. L05.

1494 Figure 11. Element enrichments and depletions of red-zone rocks. (a) Comparison of red zone on
1495 the border of Spirit of Saint Louis with host bedrock on either side; inset shows details for
1496 enriched elements. (b) Ge vs. SiO₂ for rocks around Spirit of Saint Louis compared to similar
1497 rocks from Marathon Valley. Boxes on abscissa represent approximate detection limits for Ge,
1498 which encompass most analyses from Marathon Valley.

1499 Figure 12. Alteration diagrams for Endeavour crater rim rock types, after (a) Nesbit and Wilson
1500 (1992) and (b) Meunier et al. (2013). Blue arrows show expected change for alteration under low
1501 water/rock in which olivine dissolves (Hurowitz & McLennan, 2007). White arrow joins host
1502 bedrock with red-zone rock from Spirit of Saint Louis (see Fig. 10). Curved arrows show
1503 alteration changes in Monaro basalts (Eggerton et al., 1987). Labeled pitted rock symbols are: A
1504 – Allende; N – Nazas; T – Tomé. Independence-class rocks from Gusev crater shown for
1505 comparison.

1506 Figure 13. Images of pitted Nazas target from Perseverance Valley. (a) Portion of Pancam false-
1507 color image (Sol 5042, L257) highlighting pit filled with reddish-orange alteration material. (b)
1508 Portion of Microscopic Imager image (Sol 5053) of the pit showing texture of the alteration
1509 material. The location of (a) can be found in online supplementary Fig. L09.

1510 Figure 14. Element vs. SO₃ diagrams for altered rocks and soils from the Endeavour crater rim.
1511 Red circles enclose Si-rich red-zone-group targets from Gasconade, which also includes CaSO₄-
1512 rich components (red dashed tie lines).

1513 Figure 15. (a) Pancam false-color image (Sol 4404, L257) of the wheel scuff exposing altered
1514 soils in a fracture in Shoemaker lower-1 showing locations of APXS targets. The line of red
1515 pebbles is a red zone transecting the outcrop. (b) Pancam false-color image (Sol 4504, L257) of
1516 the Gasconade vein complex (cyan arrows) cross cutting Shoemaker lower-1 on Spirit Mound;
1517 region of (c) indicated. (c) Pancam false-color image (Sol 4505, L257) of a portion of the
1518 Gasconade vein complex showing locations of APXS targets; CaSO₄-rich Gasconade and
1519 Gasconade 2, and Si-rich Gasconade 3 and Gasconade 4. The location of (a) can be found in
1520 online supplementary Fig. L07; that of (b) and (c) in Fig. L08.

1521 Figure 16. Comparison of Pancam spectra from light-toned soil exposed by Spirit rover scuff at
1522 the Arad target (MER-A Sol 721) and the yellow pebble Private Joseph Field at Opportunity's E

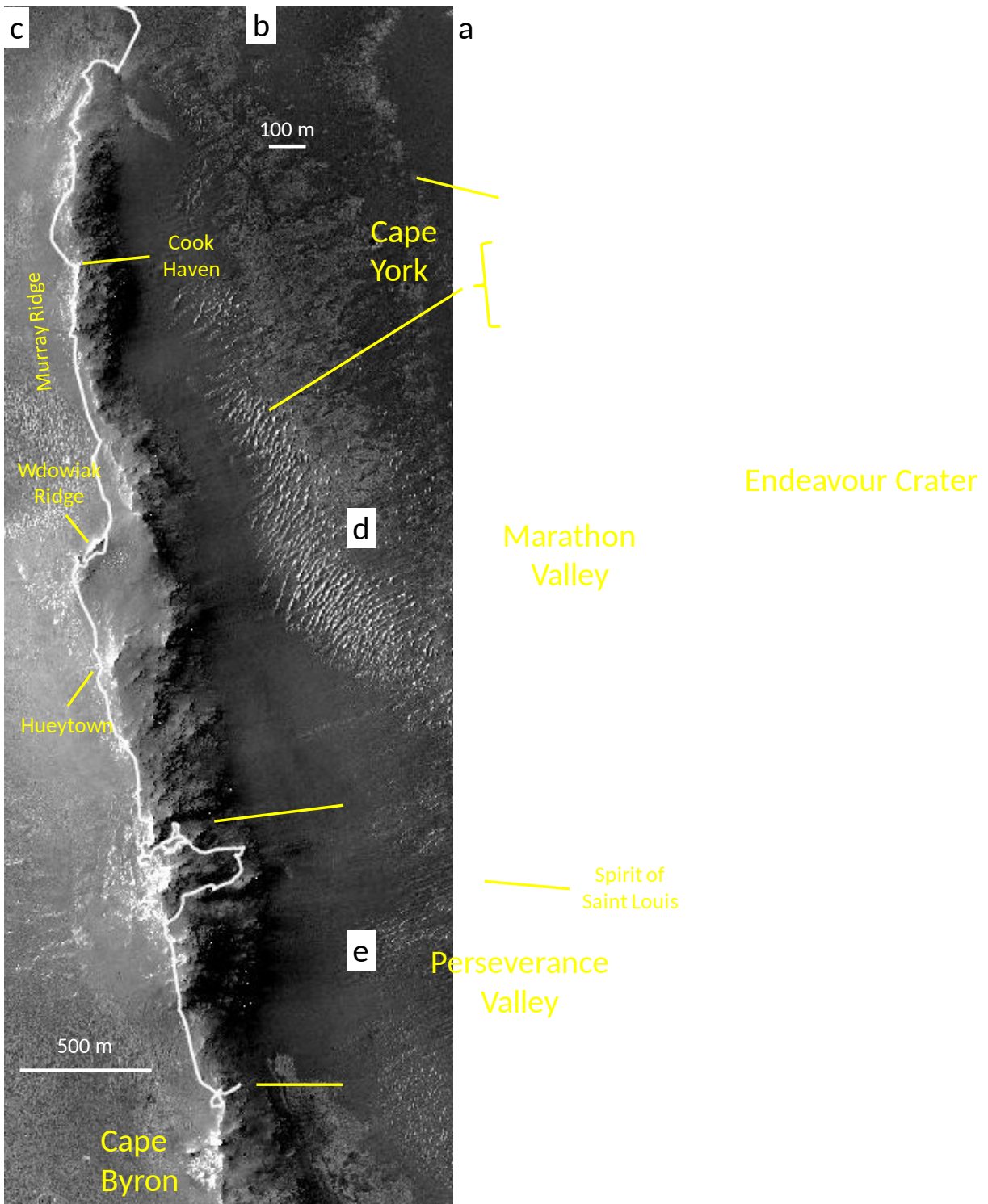
1523 Cann scuff area (MER-B Sol 4379) (Fig. 15a). Each has a broad absorption centered between
1524 803 and 864 nm attributed to Fe sulfate mineral(s). R* is relative reflectance; standard deviations
1525 are shown when larger than the symbol size.

1526 Figure 17. (a) Molar element/Si in abraded interiors normalized to brushed surfaces for select
1527 elements. (b) Molar Cl/Si vs. Ca/Si for abraded and brushed targets, with the effect of adding
1528 0.75 or 1.5 wt% CaCl₂ to interior compositions shown (see text).

1529 Figure 18. (a) Pancam false-color image (Sol 2063, L257) of the front, dusty side of Marquette
1530 Island. The front face is roughly 30×30 cm in size. (b) Pancam false-color image (Sol 2089,
1531 L257) of the relatively dust-free top of Marquette Island. Peck Bay brush circle (front face,
1532 arrow) is 45 mm in diameter. (c) MI image of the hackly top surface of Marquette Island. Arrow
1533 points out thin, possible alteration vein. Image is 31 mm across. (d) Portion of an MI image of
1534 the abrasion hole showing clastic texture. Arrow points out arcuate, possible glass shard. Image
1535 is 15.5 mm across.

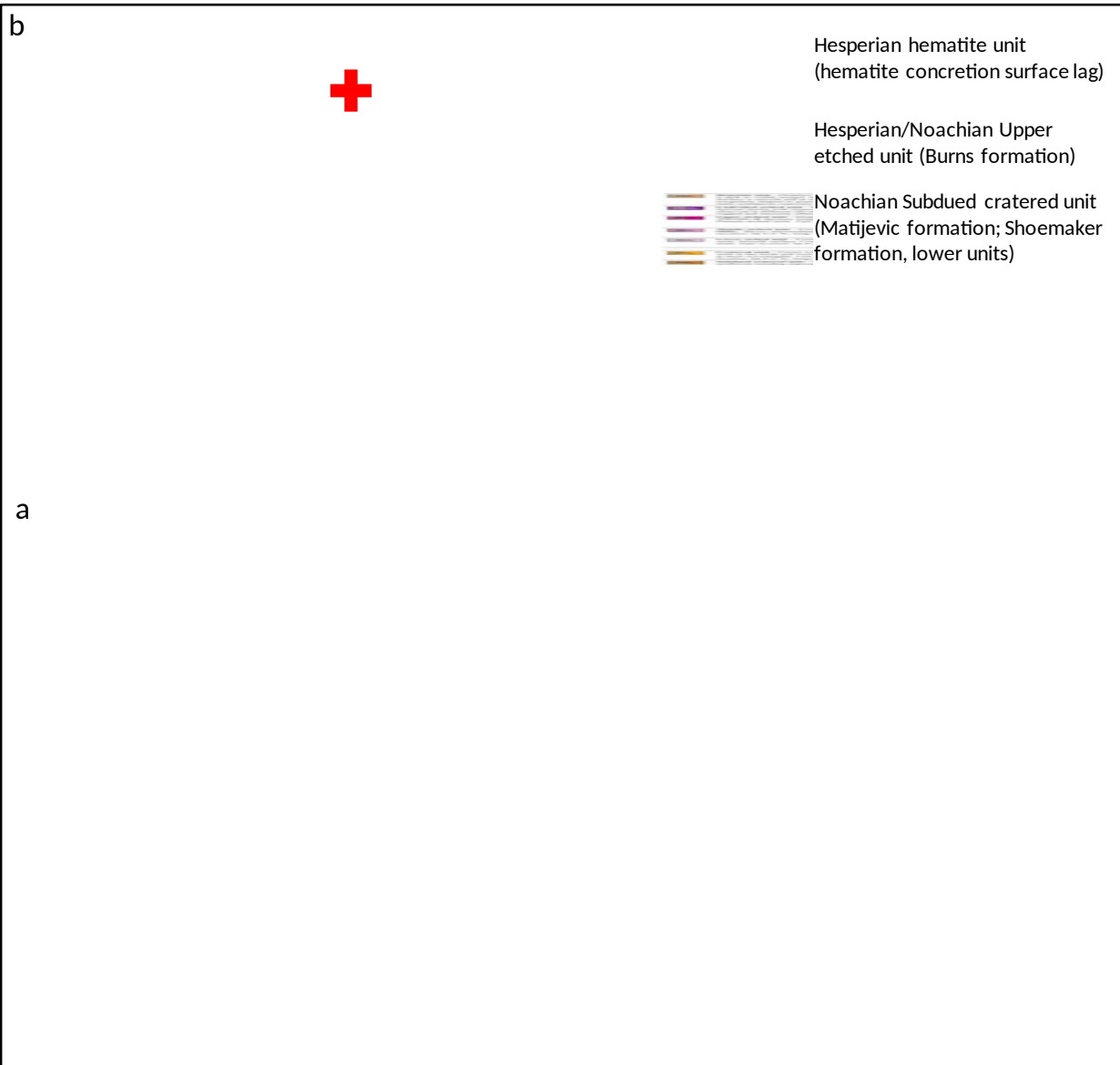
1536 Figure 19. Compton/Rayleigh scatter peak ratio for Marquette Island analyses compared to those
1537 of compositionally similar basalts.

1538



1539

1540 Figure 1.



1541

1542 Figure 2.

a

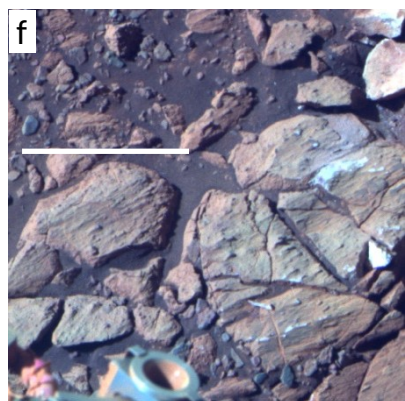
b

c

d

e

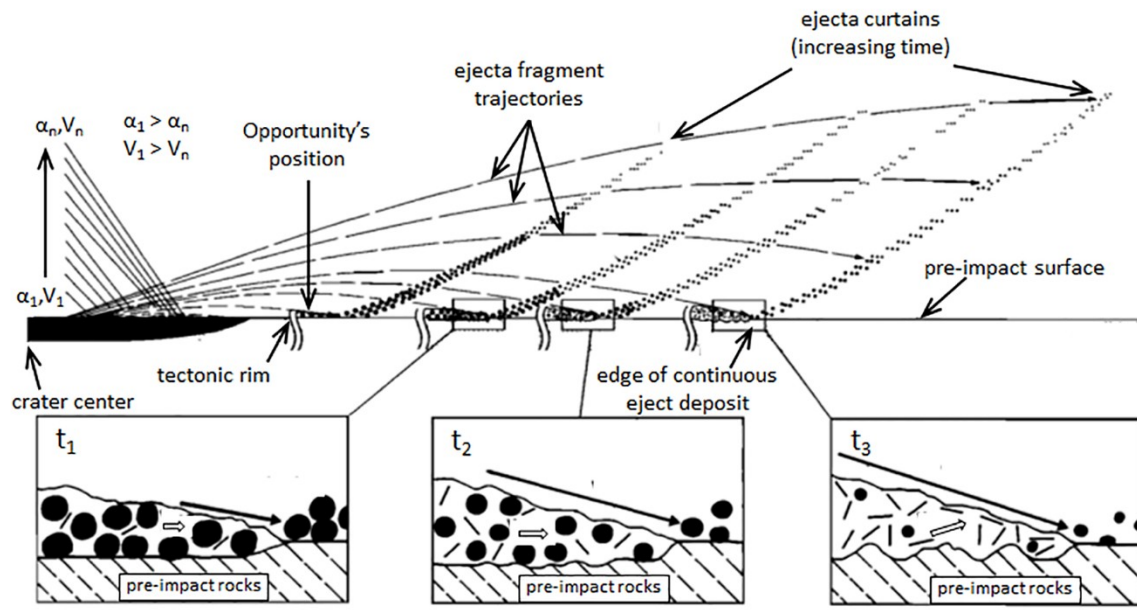
f



1543

1544 Figure 3.

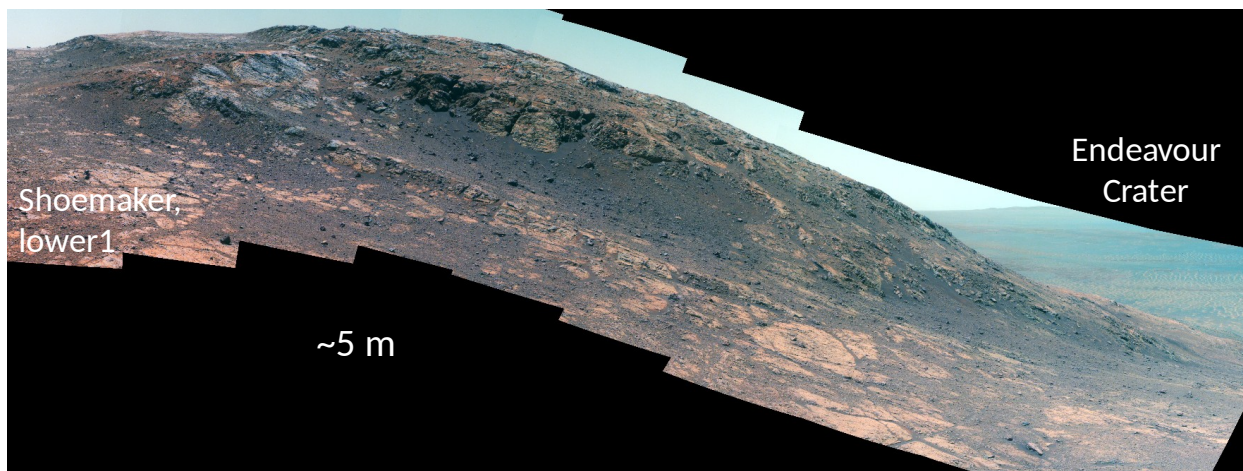
1545



1546

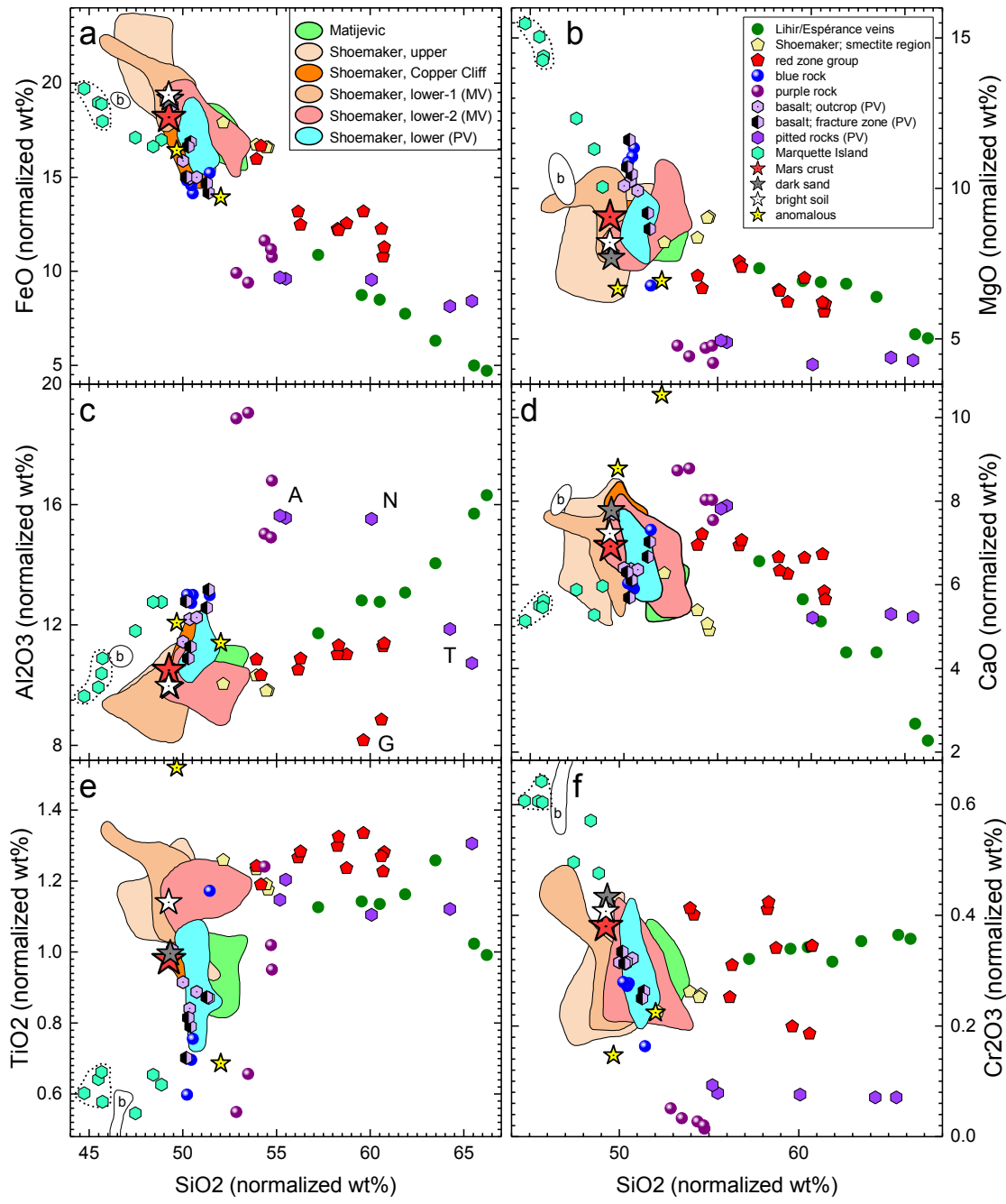
1547 Figure 4.

1548



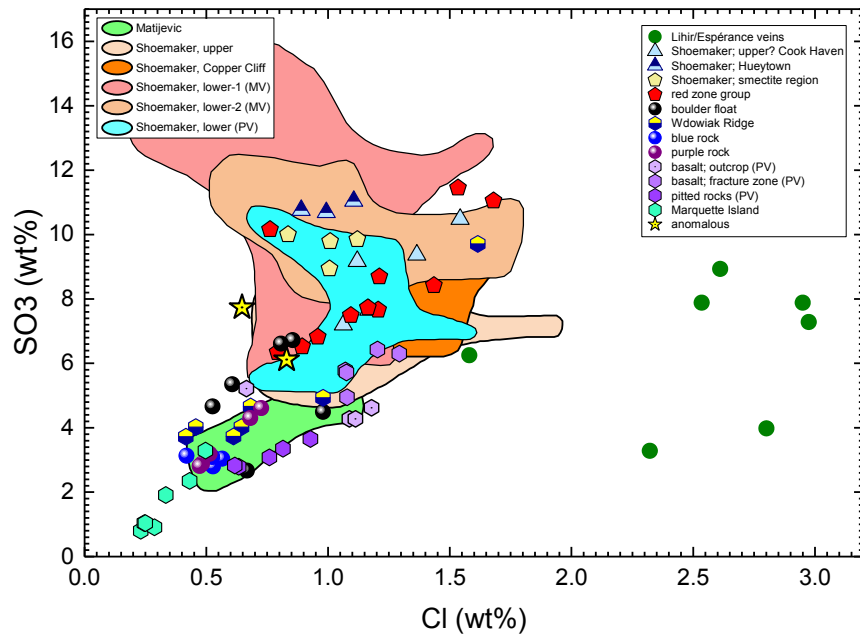
1549

1550 Figure 5.



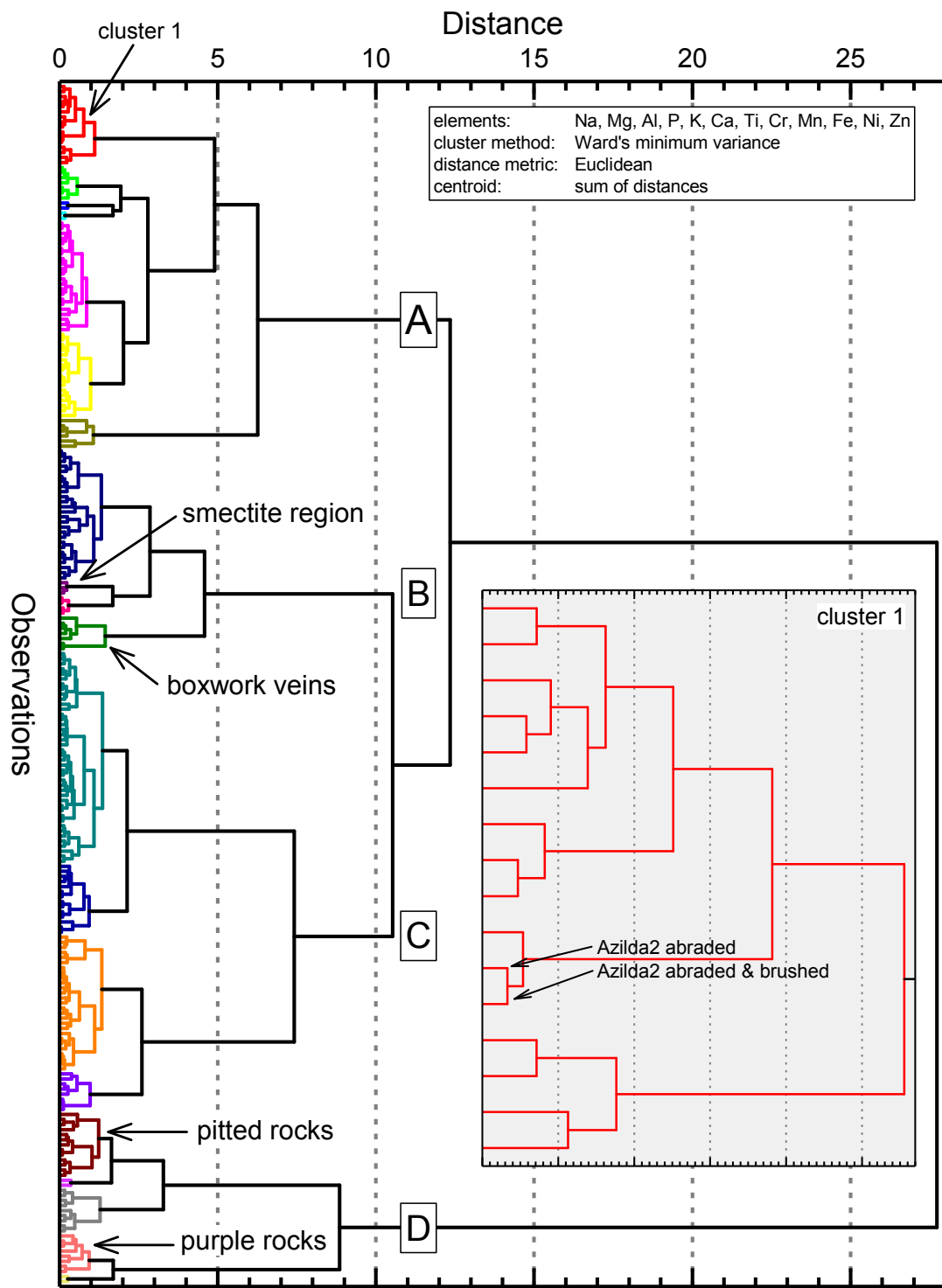
1551

1552 Figure 6.



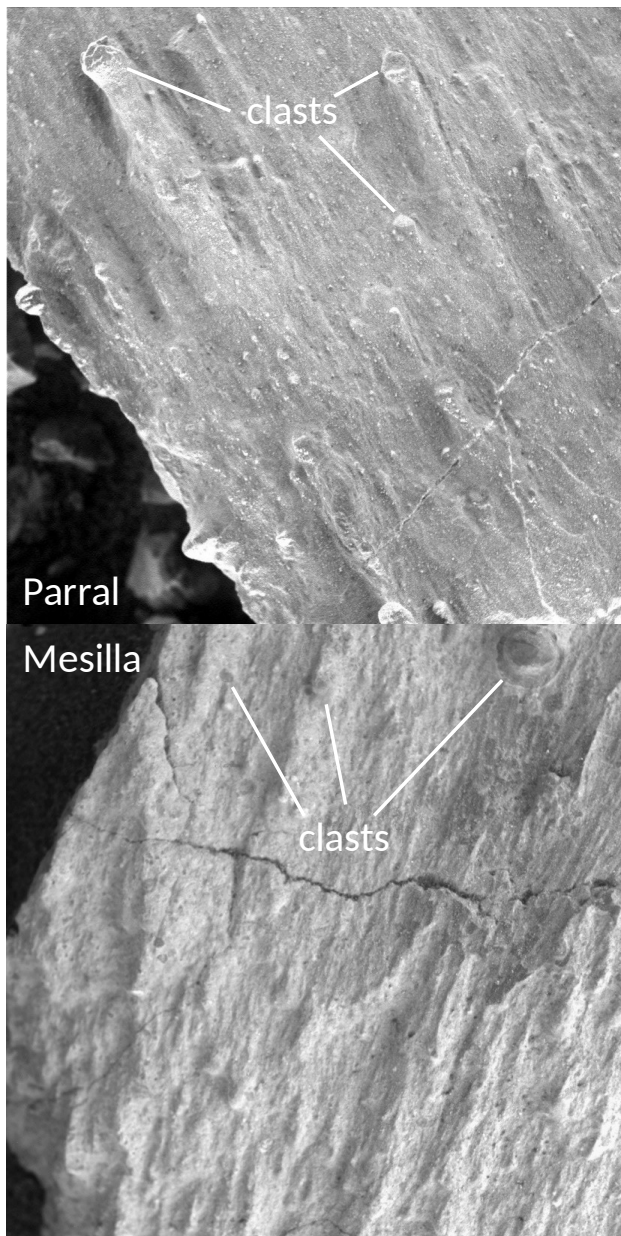
1553

1554 Figure 7.



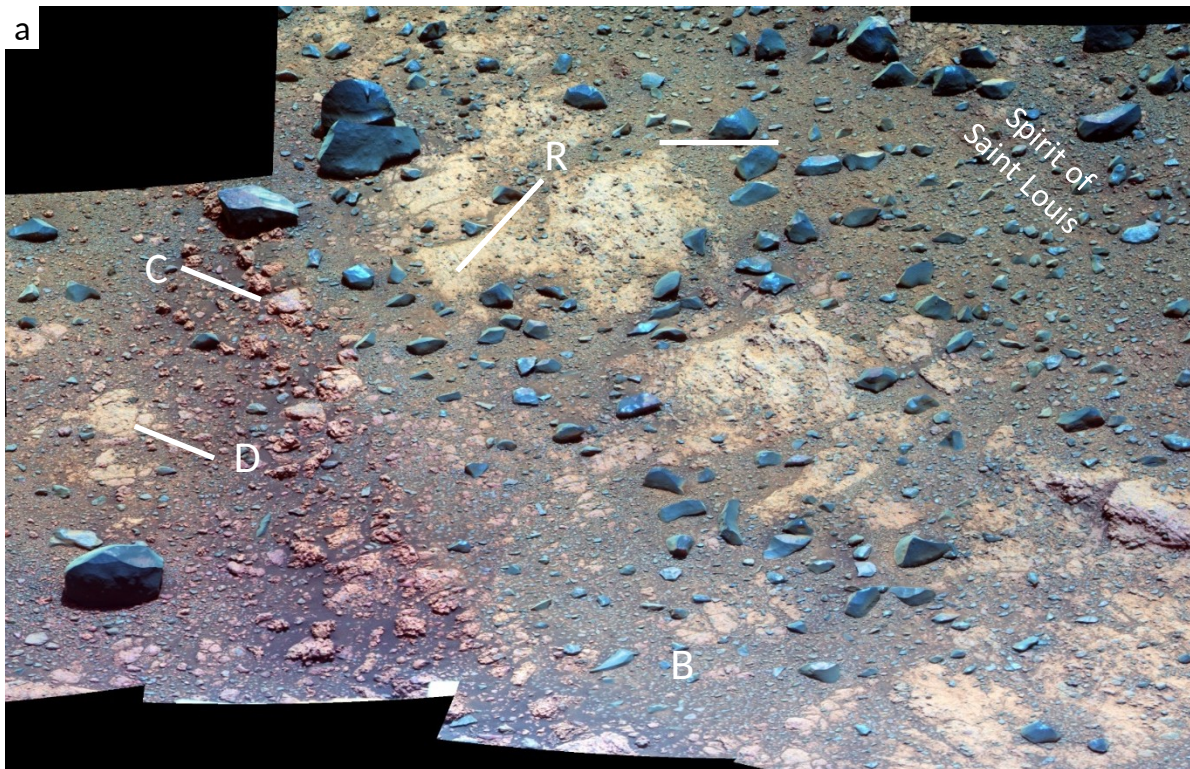
1555

1556 Figure 8.

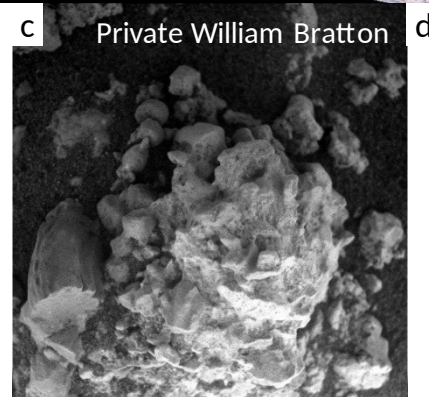


1557

1558 Figure 9.

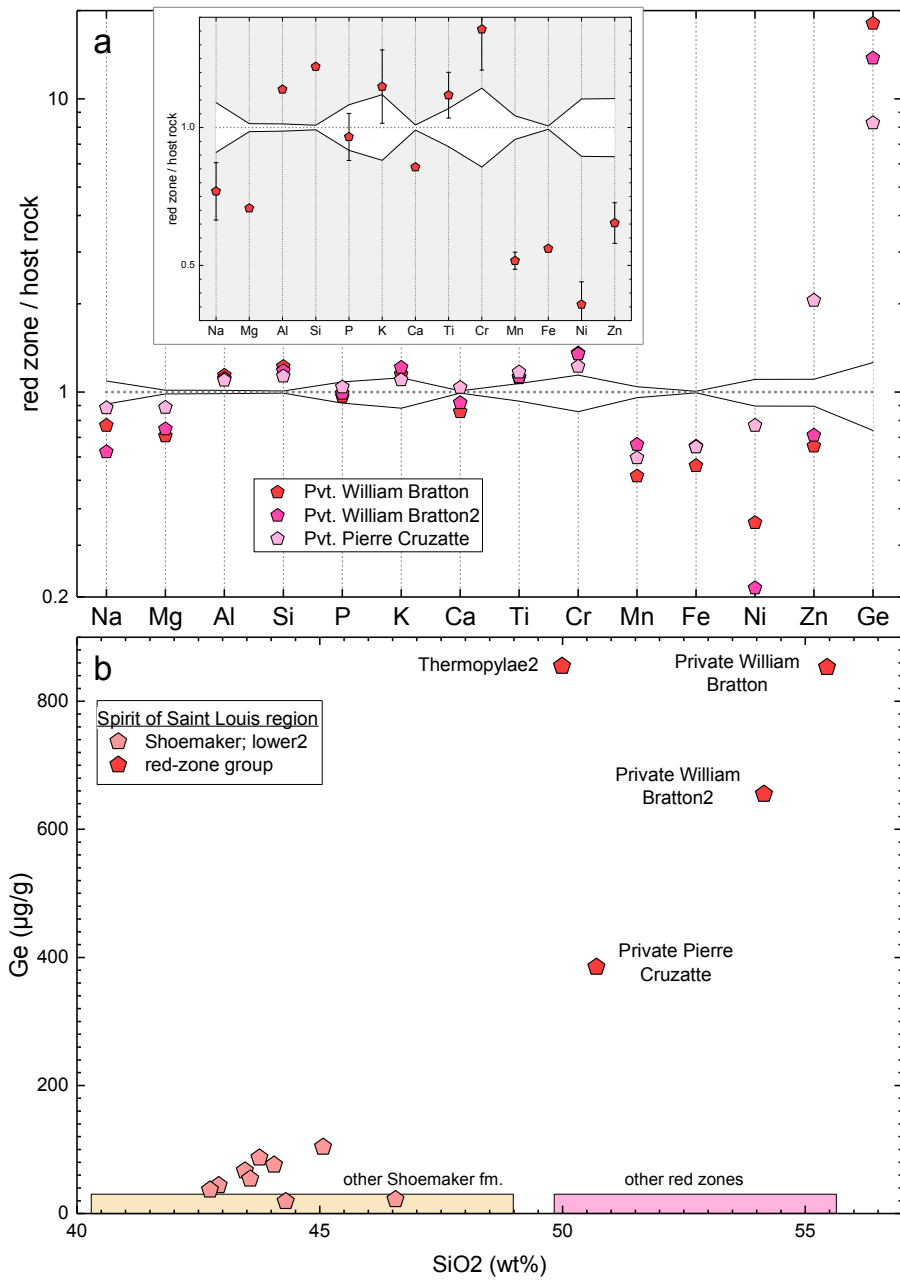


b



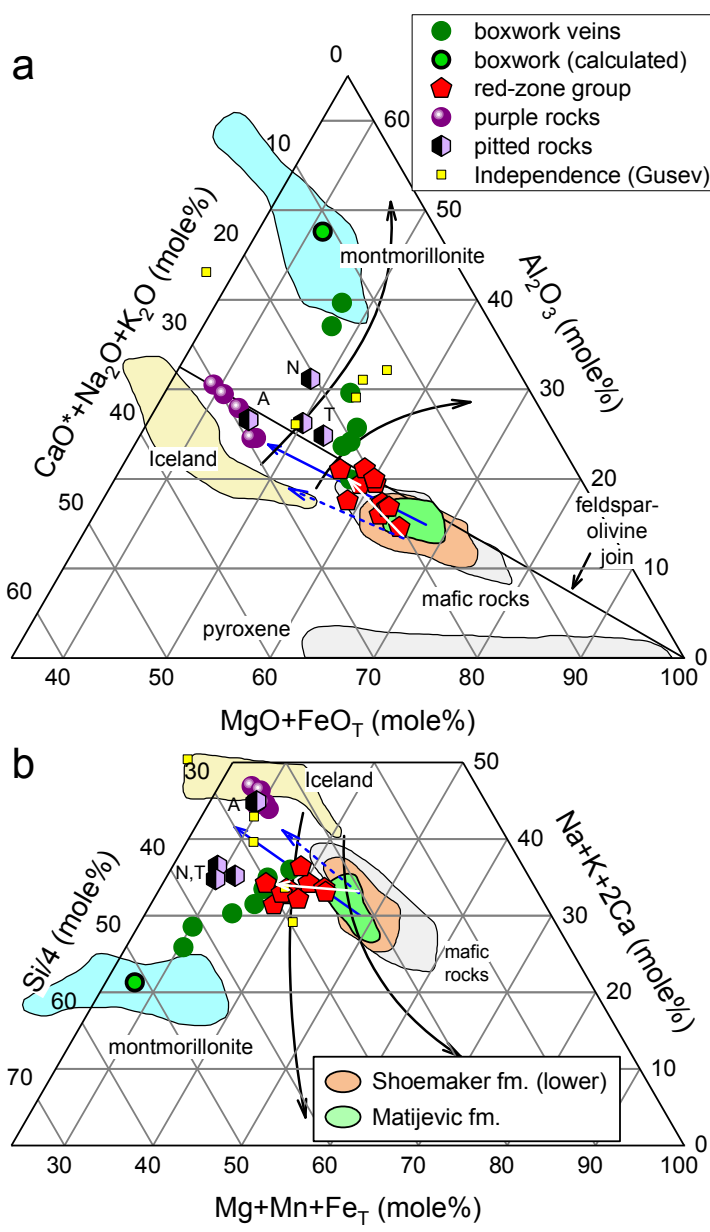
1559

1560 Figure 10.



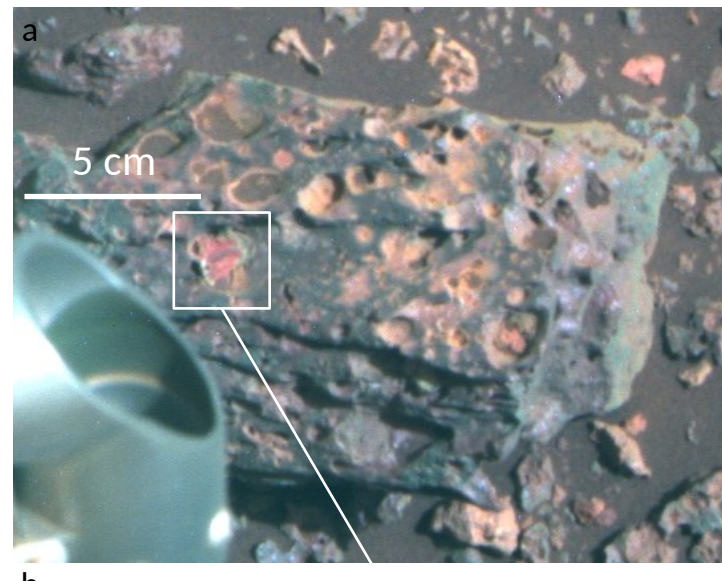
1561

1562 Figure 11.



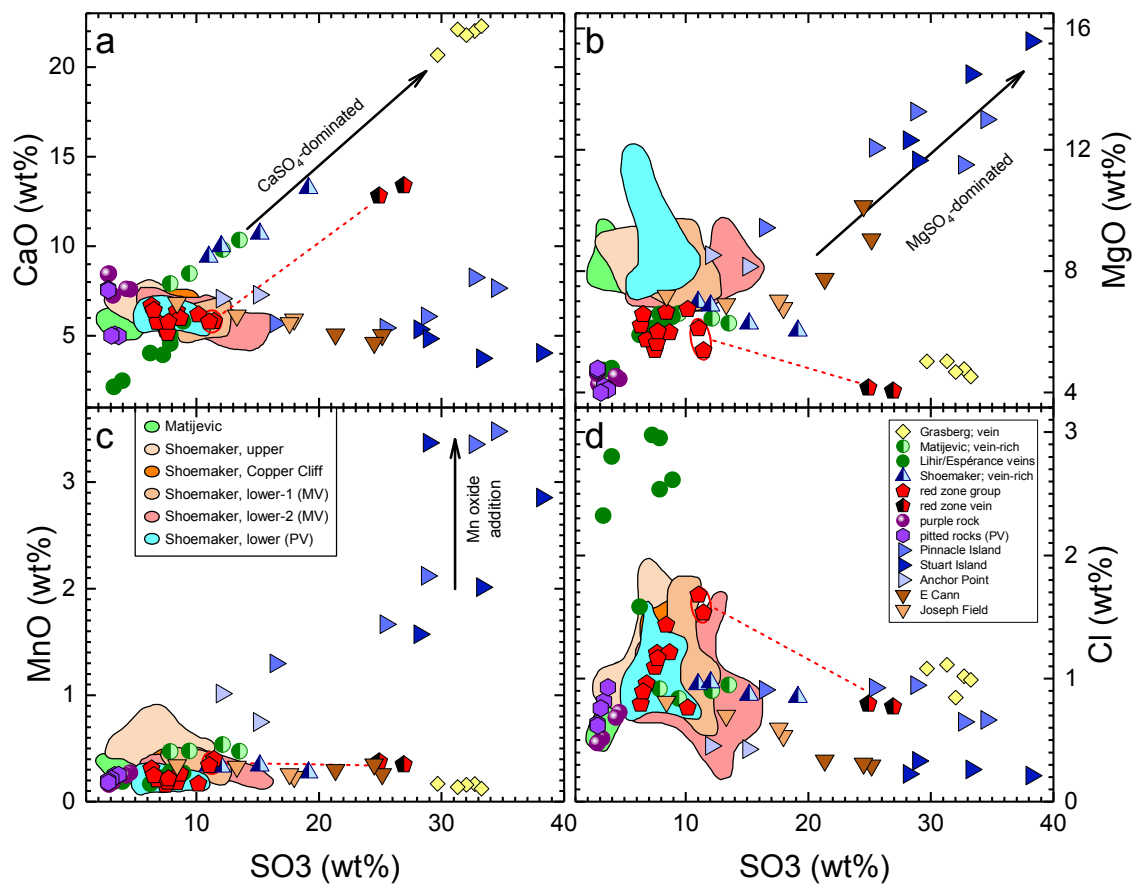
1563

1564 Figure 12.



1565

1566 Figure 13.

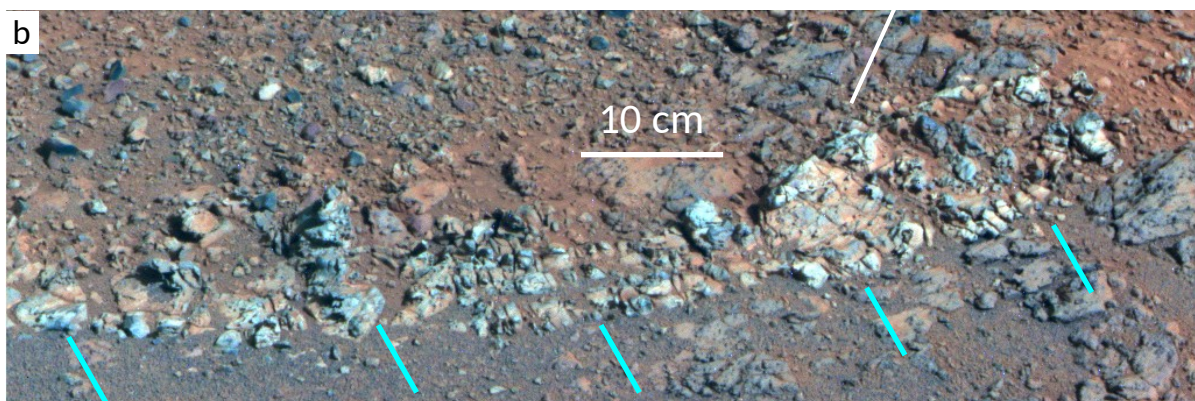


1567

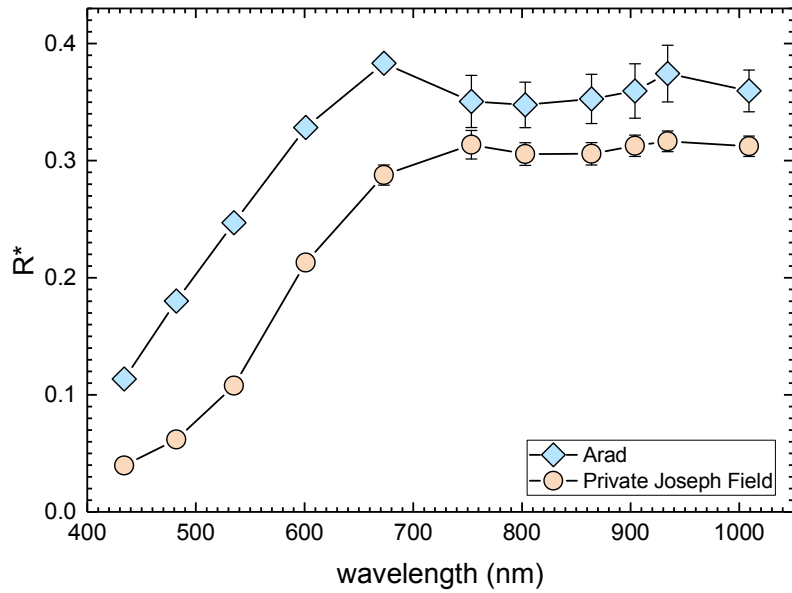
1568 Figure 14.

a

c

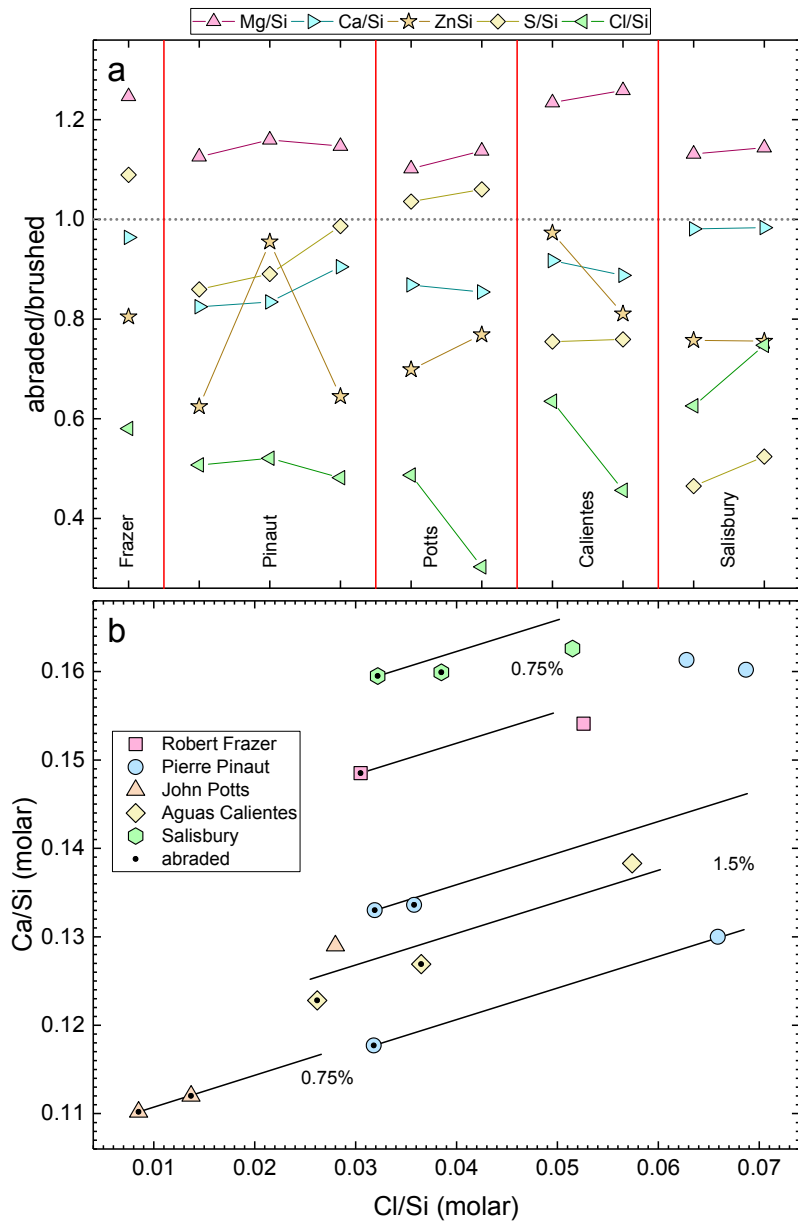


1570 Figure 15.



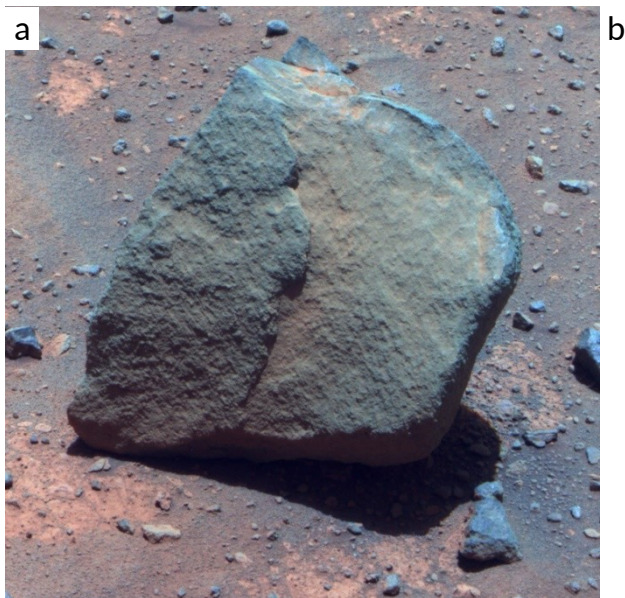
1571

1572 Figure 16.



1573

1574 Figure 17.



a

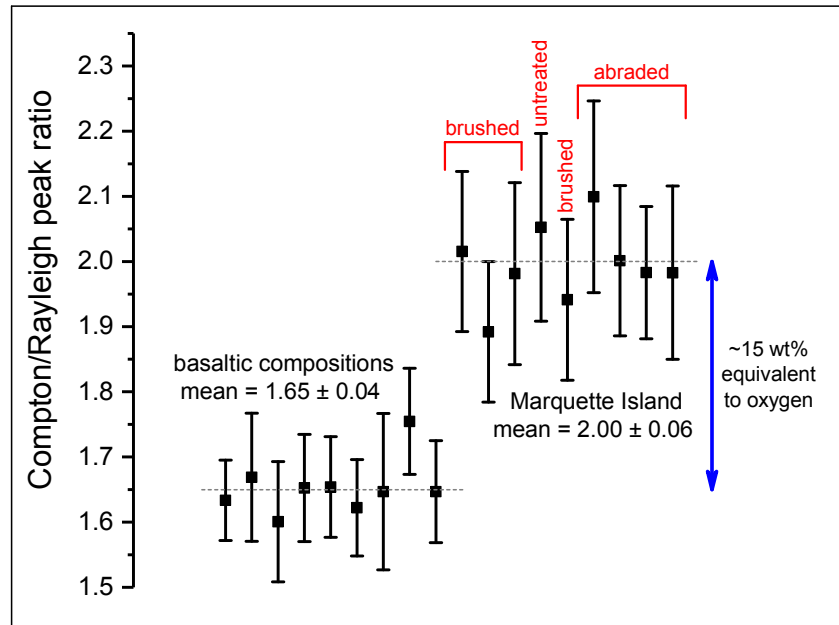
b

c

d

1575

1576 Figure 18



1577

1578 Figure 19.